

Implication of the velocity dispersion scalings on high-mass star formation in molecular clouds

AN-XU LUO,^{1,2} HONG-LI LIU,^{1,2} SHENG-LI QIN,¹ DONG-TING YANG,¹ AND SIRONG PAN¹

¹*School of physics and astronomy, Yunnan University, Kunming, 650091, PR China*

²*Both authors contributed equally to this work.*

ABSTRACT

This paper is aimed at exploring implications of velocity dispersion scalings on high-mass star formation in molecular clouds, including the scalings of Larson’s linewidth–size (σ – R) and ratio–mass surface density (\mathcal{L} – Σ ; here $\mathcal{L} = \sigma/R^{0.5}$). We have systematically analyzed the σ parameter of well-selected 221 massive clumps, complemented with published samples of other hierarchical density structures of molecular clouds over spatial scales of 0.01–10 pc. Those massive clumps are classified into four phases: quiescent, protostellar, HII region, and PDR clumps in an evolutionary sequence. The velocity dispersion of clumps increases overall with the evolutionary sequence, reflecting enhanced stellar feedback in more evolved phases. The relations of σ – R and \mathcal{L} – Σ are weak with the clump sample alone, but become evident when combined with others spanning a much wider spatial scales. For σ – R , its tight relation indicates a kinematic connection between hierarchical density structures, supporting theoretical models of multiscale high-mass star formation. From the \mathcal{L} – Σ relation, cloud structures can be found to transition from over-virial state ($\alpha_{\text{vir}} > 2$) to sub-virial state ($\alpha_{\text{vir}} < 2$) as they become smaller and denser, indicating a possible shift in the governing force from turbulence to gravity. This implies that the multiscale physical process of high-mass star formation hinges on the self-gravity of sub-virial molecular clouds. However, the influence of turbulence may not be dismissed until large-scale clouds attain a sub-virial state. This is pending confirmation from future multiscale kinematic observations of molecular clouds with uniform observing settings.

Keywords: stars: formation — stars: kinematics and dynamics; ISM: clumps.

1. INTRODUCTION

Stars form in molecular clouds (MCs) that consist of hierarchical density structures, from filaments, clumps, cores, and down to seeds of star formation. Formation of high-mass stars has been far from being understood compared to low-mass stars (Motte et al. 2018). Recently, it is increasingly accepted that high-mass star formation could be a multiscale process that proceeds on all hierarchical density structures of MCs in a top-down manner, from filaments down to seeds of star formation (e.g., Peretto et al. 2013; Motte et al. 2018; Vázquez-Semadeni et al. 2019; Liu et al. 2022a,b, 2023; Yang et al. 2023). This multiscale phenomenon could be regulated by several basic factors such as turbulence, gravity, and magnetic field of MCs.

The turbulence in MCs could drive the multiscale physical process related to high-mass star formation. Different hi-

erarchical density structures of MCs could be kinematically correlated through coherent motions across a wide range of scales, from 0.1 pc up to 100 pc, as reflected from the Larson’s linewidth–size relation (e.g., Larson 1981; Solomon et al. 1987), which is one of the empirical velocity dispersion scalings. In theory, supersonic turbulence can generate an intricate network of filaments (e.g., Inoue & Fukui 2013a; Gong & Ostriker 2015), as well as denser substructures (e.g., clumps/cores) with non-linear density fluctuations, which are the sites of star formation (e.g., Elmegreen 1993; Ballesteros-Paredes et al. 2011b; Kritsuk et al. 2011; Hennebelle & Falgarone 2012; Pan et al. 2019; Padoan et al. 2020). This implies a connection between supersonic turbulence and star formation. This connection has been strengthened by simulations of MCs with supersonic turbulence triggered by supernova explosions (Padoan et al. 2016). The simulations reproduced the power-law form of the Larson’s velocity-size relation, that is $\sigma \propto R^{0.39}$, where σ is the velocity dispersion. In this context, Padoan et al. (2020) posited high-mass stars form in MCs by a multiscale mass accretion/transfer process from large-scale converging inertial flows through

clumps and cores to seeds of star formation, where large-scale inertial flows are thought to originate from supersonic turbulence.

In addition to turbulence, gravity could regulate the multiscale dynamical scenario of high-mass star formation. The “global hierarchical collapse” (GHC) model proposed that the multi-scale accretion process in high-mass star formation is primarily governed by gravity on all scales (Vázquez-Semadeni et al. 2019). In this model, MCs evolve by hierarchical and chaotic gravitational collapse from large-scale clouds through clumps and cores down to seeds of star formation (e.g., Hartmann & Burkert 2007; González-Samaniego et al. 2014; Vázquez-Semadeni et al. 2017). This gravitational collapse is accompanied by the release of gravitational energy, which in turn generates kinetic energy (e.g., Vázquez-Semadeni et al. 2009; Ballesteros-Paredes et al. 2011a; Vázquez-Semadeni et al. 2019; Ballesteros-Paredes et al. 2020). As suggested in Vázquez-Semadeni et al. (2019), this energy conversion could be reflected from the Larson’s ratio–mass surface density (\mathcal{L} – Σ) relation (see below for more discussions), another velocity dispersion scaling, where \mathcal{L} is define as $\sigma/R^{0.5}$. Moreover, the global hierarchical collapse of cloud structures was claimed to facilitate formation of high-mass stars.

Recent observations have provided evidence for a multiscale scenario of high-mass star formation, highlighting the significance of both turbulence and gravity in this process (Liu et al. 2022a,b, 2023; Zhou et al. 2022; Yang et al. 2023; Pan et al. 2024). For instance, Yang et al. (2023) and Pan et al. (2024) observed a multiscale, dynamical mass accretion process in two different hub-filament system clouds (i.e., G310 and G34). Such observational evidence supports the latest generation of GHC and I2 models, but they differ in driving mechanisms for this scenario, particularly on the larger scales. The GHC model supports a gravity-driven hierarchical process, whereas the I2 model suggests a turbulence-driven mechanism. This disparity was also observed in previous investigations of a filamentary infrared dark cloud, G34, at ~ 2 arcsecond resolution (e.g., Liu et al. 2020, 2022a,b). Those authors argued that the scale-dependent combined effect of turbulence and gravity is crucial for high-mass star formation in the cloud. Therefore, a comprehensive observational study of the interaction between turbulence and gravity in a large sample of cloud structures is necessary. As mentioned earlier, the velocity dispersion scalings would be an useful approach for such study.

This paper presents a study primarily on the gas kinematics (i.e., velocity dispersion) of 221 massive star-forming clumps. The H^{13}CO^+ (1–0) molecular line is used as a tracer of the velocity dispersion. The goal is to understand the multiscale high-mass star formation scenario from the velocity dispersion scaling across all hierarchical density structures of

MCs. To this end, our data set of massive clumps are complemented with samples of other hierarchical density structures from the literature (see below). The paper is structured as follows: Section 2 describes the main data sets used in this study; Section 3 presents the results and analysis; Section 4 discusses the main findings; and Section 5 summarizes the conclusions.

2. DATA SET

The Millimetre Astronomy Legacy Team 90 GHz (MALT90) survey is a molecular line survey at 90 GHz that aims to characterize the physical and chemical evolution of massive star-forming clumps (Jackson et al. 2013). This survey observed a total of 3,246 massive star formation clumps using the Mopra 22m-aperture single-dish telescope at an angular resolution of $\sim 38''$ and a sensitivity of 0.25 K for the 0.11 km s^{-1} velocity resolution. The targeted clumps are a subsample of the sources observed by the ATLASGAL 870 μm dust continuum survey (Schuller et al. 2009), and are distributed in a range of $300^\circ \leq l \leq 20^\circ$ and $|b| \leq 1^\circ$. The MALT90 survey simultaneously observed 16 major molecular lines at 90 GHz, providing a detailed, legacy catalog of molecular line emission for massive star formation clumps (Rathborne et al. 2016). Among the 16 major lines, the $J=1-0$ transitions of HCO^+ and H^{13}CO^+ lines, which serve as tracers of dense gas (Jackson et al. 2013), are primarily focused here.

In addition, the 870 μm dust continuum data from the ATLASGAL survey (Schuller et al. 2009), and the mid-infrared images (3.6, 4.5, 5.6, 8.0, and 24 μm) from the *Spitzer*-GLIMPSE (Churchwell et al. 2009) and -MIPSGAL (Carey et al. 2009) surveys are used to investigate the IR signatures of the star-formation activity of the massive clumps studied here.

3. RESULTS AND ANALYSIS

3.1. Sample refinement

We applied certain criteria to refine the sample of clumps for robust kinematic analysis (i.e., velocity dispersion, σ). Firstly, we excluded those clumps located in $|l| \leq 10^\circ$ from the initial set of 3,246 sources observed in the MALT90 survey. These clumps generally have a complex velocity nature that could lead to a highly inaccurate σ measurement.

From the inspection of the clump-averaged H^{13}CO^+ (1–0) spectrum, we eliminated those clumps with multiple velocity components along the line of sight that can also affect the measurement’s accuracy. From the line spectrum, several observed parameters, such as σ and the line peak intensity, I_p , can be measured performing a Gaussian fit to the averaged H^{13}CO^+ spectrum over the effective clump radius catalogued in Guzmán et al. (2015). Those authors defined the

effective radius as $\theta_{\text{eff}} = \sqrt{\Omega/\pi}$ where Ω corresponds to the area with mass surface densities greater than 0.01 g cm^{-2} .

Based on the measurement of the line peak intensity of H^{13}CO^+ , we discarded those clumps with I_p below 3 rms, where the rms was estimated in a 5.5 km s^{-1} wide spectral window free of line emission. As a result, we obtain a refined sample of 249 clumps. Note that a final sample of 221 clumps are used for robust kinematic analysis (see Sect. 3.2).

3.2. Clump classification

Following Rathborne et al. (2016), we re-examined the evolutionary phases of the massive clumps investigated here, by adopting a classification scheme based on infrared (IR) signatures, as discussed in the literature (e.g., Chambers et al. 2009; Guzmán et al. 2015). To this end, we utilized the *Spitzer* images at 3.6, 4.5, 5.8, 8.0, and $24 \mu\text{m}$. According to Rathborne et al. (2016), five candidate phases of clumps are determined as follows: 1) quiescent clumps, which are IR-dark in all *Spitzer* 3– $24 \mu\text{m}$ images; 2) protostellar clumps, which are associated either with a point-like source indicative of a young stellar object (YSO) at least in one of the *Spitzer* images, or with extended $4.5 \mu\text{m}$ emission indicative of the shocks generated by an associated YSO(s); 3) HII region clumps, which are characterized as a compact clumpy $8 \mu\text{m}$ signature typical of polycyclic aromatic hydrocarbon (PAH) emission related to ionized gas from newly born massive stars; 4) photodissociation region (PDR) clumps, which are dominated by extended $8 \mu\text{m}$ PAH emission typically appearing at the interface between ionized and molecular gas; 5) uncertain clumps, which have ambiguous IR signatures, and thus cannot be grouped into any of the four known phases. In Appendix A, we provide examples of the classification scheme, showing how different IR signatures between 3.6 and $24 \mu\text{m}$ correspond to the candidate evolutionary phases of clumps.

As a result, the classification scheme yields five candidate phases of clumps, including 18 quiescent, 100 protostellar, 84 HII region, 19 PDR, and 28 uncertain phases. To explore the velocity dispersion as a function of evolution phase (see below), we hereafter will take into account only the 221 known-phase clumps for robust analysis. Their major parameters mentioned above are listed in Table 1 of Appendix B, including the radius (R), mass surface density (Σ), mass (M), luminosity (L), and velocity dispersion (σ) in order from Col. 5 to Col. 9.

The bolometric luminosity-mass ratio (L/M) is a commonly-used indicator of clump evolution (Molinari et al. 2008). For the 221 clumps investigated here, their luminosity can be retrieved from Contreras et al. (2017) and Urquhart et al. (2022) who derived it from the spectral energy distribution (SED) fitting to the observed fluxes at least in three wavelength bands between $8 \mu\text{m}$ and $870 \mu\text{m}$ (Urquhart et al.

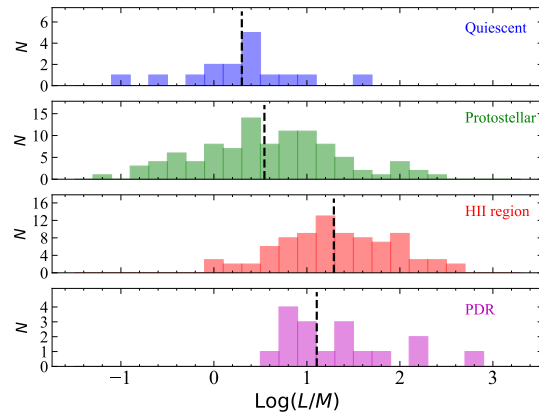


Figure 1. Luminosity-mass ratio distribution for different evolutionary phases of clumps, including the quiescent, protostellar, HII region, and PDR phases. The black vertical dashed line marks the median ratio for each phase. The median value for each phase is 2.0, 3.5, 19.5, 12.8, respectively.

2018). The calculation of the clump mass is referred to Sect. 3.3.

Figure 1 presents the L/M distribution of the clumps for different evolutionary phases. Note that three clumps (AGAL012.863-00.244, AGAL013.213+00.039, and AGAL014.626-00.562) do not have available luminosity measurements, and thus are not considered in the figure. Overall, the L/M of these clumps increases from the quiescent to HII region phase, as manifested by the median ratio of each phase (see the dashed line in Figure 1). This result is in good agreement with that of the evolutionary classification from the IR signatures (see above). It is worth noting that there is no significant difference in the L/M distribution between the HII region and PDR clumps. This implies that these two phases of clumps investigated here do not differ significantly from each other. However, they still have the average L/M ratios much higher than the other two phases of clumps, as reflected from the median ratio value of the phases in Fig. 1.

3.3. Clump mass and mass surface density

The mass surface density Σ and effective radius R of 221 massive clumps investigated here have been estimated by Guzmán et al. (2015). These parameters were derived from the SED fitting to the photometric fluxes at least in three wavelengths of *Herschel* 160, 250, 350, and $500 \mu\text{m}$, and ATLASGAL $870 \mu\text{m}$. We calculated here the clump mass as $M = \pi R^2 \Sigma$.

The 221 clumps have 27 to $64,978 M_{\odot}$ for the mass, and 0.04 to 0.42 g cm^{-2} for the mass surface density. They have median values of [379, 1061, 1611, 1761] M_{\odot} for the mass, and [0.12, 0.13, 0.12, 0.12] g cm^{-2} for the mass sur-

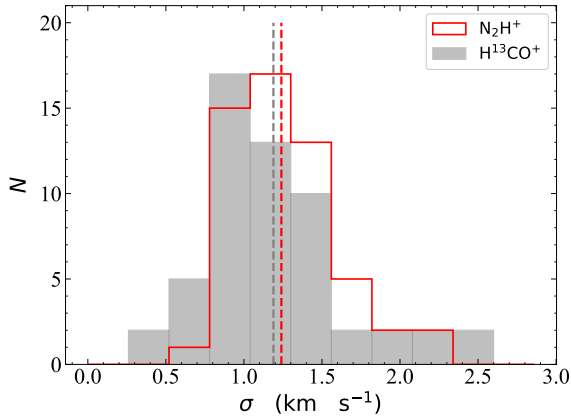


Figure 2. Velocity dispersion distribution of the 55 clumps that overlap between [Traficante et al. \(2018\)](#) and this work. The gray and red histograms represent the velocity dispersion distributions derived from the H^{13}CO^+ (1–0) line (see Sect. 3.1), and the N_2H^+ (1–0) line ([Traficante et al. 2018](#)), respectively. In turn, the gray and red dashed lines correspond to the mean values of the two distributions, respectively.

face density, from the quiescent, protostellar, HII region, and PDR phase, respectively. These results suggest that most of the clumps investigated here, if not all, are sufficiently massive and dense for high-mass star formation, as requested by an empirical high-mass star formation threshold of $\Sigma_{\text{crit}} \geq 0.05 \text{ g cm}^{-2}$ (e.g., [Urquhart et al. 2014](#)).

3.4. Velocity dispersion

In our samples, there are 55 clumps that overlap the targets analyzed by [Traficante et al. \(2018\)](#) using the N_2H^+ (1–0) line emission. For these clumps, Fig. 2 displays the comparison of the velocity dispersion distribution between the measurements from two different molecular lines. It turns out that the σ measurements from both the H^{13}CO^+ (this work) and N_2H^+ ([Traficante et al. 2018](#)) lines present a consistent distribution. Quantitatively, the velocity dispersion distribution obtained from the $\text{H}^{13}\text{CO}^+/\text{N}_2\text{H}^+$ lines shows median values of $1.2 \text{ km s}^{-1}/1.1 \text{ km s}^{-1}$, the mean values of $1.24 \text{ km s}^{-1}/1.19 \text{ km s}^{-1}$, and rms values of $0.33 \text{ km s}^{-1}/0.45 \text{ km s}^{-1}$.

In Figure 3, we present the velocity dispersion distribution (σ) of the four evolutionary phases of clumps. As can be seen, the velocity dispersion increases distinctively with the evolutionary sequence from the quiescent to HII region phase (see the dashed line for the median value in Fig. 3). This suggests that the velocity dispersion in massive star formation regions can evolve with time, and accordingly could be significantly enhanced by stellar feedback, such as protostellar jets, outflows and the expansion of ionized gas (e.g., [Knee & Sandell 2000](#); [Matzner 2002](#); [Quillen et al. 2005](#); [Goldbaum](#)

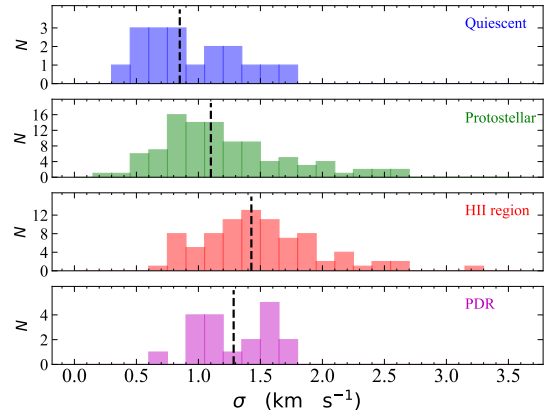


Figure 3. Velocity dispersion distribution for different evolutionary phases of clumps, including the quiescent, protostellar, HII region, and PDR phases. The black vertical dashed line indicates the median value for each phase. The median value for each phase is 0.8 km s^{-1} , 1.1 km s^{-1} , 1.4 km s^{-1} , 1.3 km s^{-1} , respectively. The velocity dispersion increases from the quiescent to HII region phase, but then decreases toward the PDR phase.

[et al. 2011](#)). Moreover, the decrease in the velocity dispersion of the PDR clumps can be found compared to the HII-phase counterparts. This could be due to the fact that PDRs are generally located farther away from the central massive star than HII regions, and thus could be less affected by strong stellar feedback. Even so, the velocity dispersion is still higher in the PDR clumps than in the quiescent and protostellar phases, which agrees with the result derived from the L/M ratio distribution.

3.5. Virial parameter

To determine the gravitational state of clumps, the virial parameter was gauged by $\alpha_{\text{vir}} = 5\sigma^2 R/(GM)$ ([Bertoldi & McKee 1992](#); [Kauffmann et al. 2013](#)), where the clump mass, radius, and velocity dispersion (M , R , and σ) can be found in Table 1, and G is the gravitational constant. The critical value of $\alpha_{\text{vir,crit}} \simeq 2$ is assumed for the hydrostatic equilibrium of spherical cloud fragments that are not supported by magnetic pressure. Therefore, clumps with $\alpha_{\text{vir}} > 2$ could be over-virial, while those with $\alpha_{\text{vir}} < 2$ could be sub-virial ([Kauffmann et al. 2013](#)).

For our sample, the α_{vir} values range from 0.11 to 11.65, spanning two orders of magnitude, with a median value of 1.13. Of the 221 clumps, 43 are of $\alpha_{\text{vir}} > 2$ while 178 are of $\alpha_{\text{vir}} \leq 2$. This suggests that the majority of the clumps are sub-virial provided that they are not supported by magnetic fields. The median α_{vir} values are observed to be [1.07, 0.96, 1.35, 0.94] in the quiescent, protostellar, HII region, and PDR phases of clumps, respectively. The protostellar clumps seem to have lower α_{vir} values than the quiescent

clumps. Note that the quoted median values between both stages of clumps differ only by 0.11, which may not be statistically significant, provided the uncertainties in estimating the masses, sizes, and velocity dispersion. Moreover, the HII region clumps have the highest virial parameters, implying fresh kinetic energy injections into clumps from embedded stellar feedback (Matzner 2002). Moving onward to the PDR phase, their α_{vir} values start to decrease, which can be attributed to their lower velocity dispersion than in HII clumps as mentioned in Sect. 3.4.

3.6. Larson’s linewidth-size relation

The Larson’s linewidth-size relation, discovered in Larson (1981), is characterised as a power-law pattern for the velocity dispersion σ and the radius R of MCs, $\sigma \propto R^\gamma$ for $\gamma = 0.38$. Later, the index γ was modified to be about 0.5 (e.g., Solomon et al. 1987; Heyer & Brunt 2004). The Larson’s σ - R relation is generally interpreted as a turbulent energy cascade from large to smaller scales in MCs, where turbulence is thought to act against gravitational collapse of MC density structures.

Figure 4 shows the σ - R distribution for our sample. We find a weak correlation between the σ and R parameters, which agrees with a lower value of the Pearson’s correlation coefficient, $\rho = 0.43$. This result does not seem to obey the Larson’s σ - R relation. However, it is worth noting that our sample covers a limited range of radii, and thus the tight σ - R relation/correlation cannot emerge. Li et al. (2023) obtained the similar result for the same analysis in a limited dynamical range of spatial scales. Moreover, if the whole sample is divided into the four phases of clumps (see Figure 4), they will not present any degree of the σ - R correlation. We therefore cannot explore how the Larson’s σ - R relation varies with star-formation environment.

To address the issue of a limited range of spatial scales when investigating the σ - R relation, we collected the data of the σ and R parameters from the literature, including Heyer et al. (2009) for a sample of GMCs in the relatively high-density area enclosed within 1/2 maximum isophote of H_2 column density, Traficante et al. (2018) for a sample of massive clumps where the overlapping 55 sources are replaced with ours, Ohashi et al. (2016) for a sample of high-mass star formation clumps and cores where we only keep those with the measurements of both σ and R , and Peretto et al. (2006), Lu et al. (2018), and Li et al. (2023) for additional high-mass star-formation cores. Using the same approach as in Sect. 3.5, the α_{vir} parameter was estimated for these new added density structures given their mass from the literature listed above.

As shown in Figure 5, the new added cloud structures from the literature enable analysis of the σ - R relation in three orders of magnitude of spatial scales. We find that the σ - R

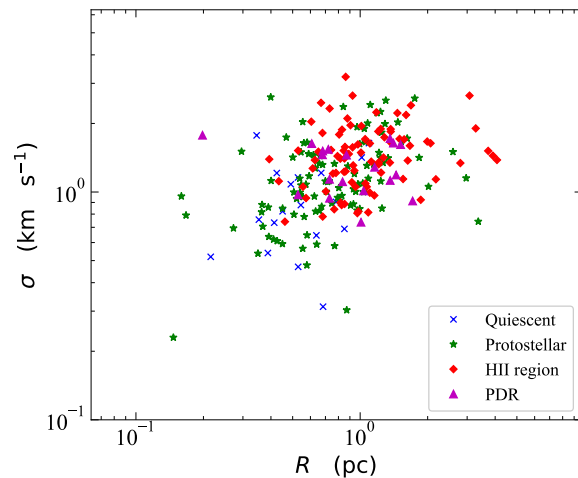


Figure 4. Velocity dispersion-radius relation for 221 massive clumps.

correlation turns tight for all of the cloud structures as characterized by a Pearson’s correlation coefficient of $\rho = 0.85$. The corresponding least squares fit in log-log space yields a slope of $\gamma = 0.31$. If all of the cloud structures are divided into two categories by the critical $\alpha_{\text{vir,crit}} = 2$, both of those with $\alpha_{\text{vir}} > 2$ and with $\alpha_{\text{vir}} < 2$ are still tightly correlated in the σ - R distribution with $\rho \geq 0.75$. They can be fitted with a power law for a slope of $\gamma = 0.26 \pm 0.04$, and $\gamma = 0.30 \pm 0.03$, respectively. Overall, for all the cloud structures as a whole or for two subsamples separated by their α_{vir} values, the derived slopes of the σ - R relation are similar (i.e., $\gamma \sim 0.30$), but shallower than the universal Larson’s relation. This result suggests that if the slopes were a result of turbulence in molecular cloud structures, the turbulent energy would cascade with a decreasing scale shallower than that reflected from the universal Larson’s relation, which could be due to additional inputs of turbulent motions for example by local star-forming feedback (e.g., stellar winds, outflows) especially on smaller scales such as clumps and cores (see Sect. 4.1). Note that this shallower slope could also be a natural consequence of the cloud collapse since it can increase non-thermal motions of the cloud, which are more structured than random turbulence (e.g., Vázquez-Semadeni et al. 2007; Ballesteros-Paredes et al. 2011a, 2018; Ibáñez-Mejía et al. 2016, 2022). Disentangling between these two types of consequences requires more dedicated investigations, which are beyond the scope of this work.

3.7. \mathcal{L} - Σ relation

The dynamics of MCs can be regulated by global gravitational collapse as inferred from the \mathcal{L} - Σ scaling relation that follows $\mathcal{L} = \sigma/R^{0.5} \propto \Sigma^{0.5}$ (Heyer et al. 2009). We inspected the \mathcal{L} - Σ relation only for our sample of massive

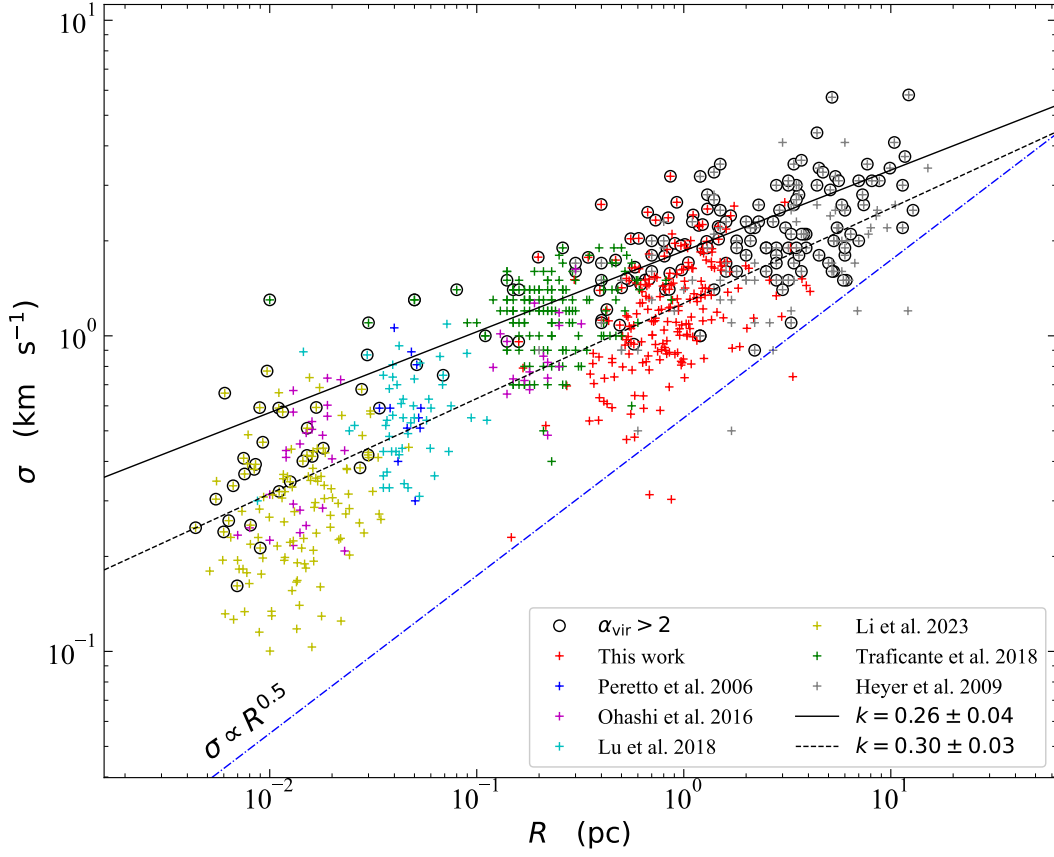


Figure 5. Velocity dispersion-radius relation for different density structures from GMCs to dense cores. The sources with $\alpha_{\text{vir}} > 2$ are circled in black, while those with $\alpha_{\text{vir}} < 2$ are not. The black solid line is the linear regression fit to the data points with $\alpha_{\text{vir}} > 2$, for a best fit slope of 0.26 ± 0.04 and a Pearson’s coefficient of $\rho = 0.75$. The black dashed line is the same but for the data points with $\alpha_{\text{vir}} < 2$, for a best fit slope of 0.30 ± 0.03 and a Pearson’s coefficient of $\rho = 0.78$. For comparison, the universal Larson’s relation is represented by the dash-dotted line.

clumps (not shown here), and found no strong correlation (the Pearson’s coefficient $\rho = 0.42$) due to the limited dynamical range of the Σ parameter. Therefore, we plot in Fig. 6 the \mathcal{L} – Σ relation with a larger dynamical range of Σ by including other cloud structures (see Sect. 3.6) in addition to our sample. As a result, a strong correlation between \mathcal{L} and Σ in the log-log space can be found with the Pearson’s coefficient $\rho = 0.83$.

We find an increasing trend of the \mathcal{L} ratio with Σ . This trend corresponds to the transition from the cloud structures of $\alpha_{\text{vir}} > 2$ to those of $\alpha_{\text{vir}} < 2$ with the former having lower \mathcal{L} ratios than the latter. Here the former structures contain mostly (64.6%) large-scale clouds while the latter consist mostly (85%) of small-scale clumps and cores. Quantitatively, the median value of the virial parameter is 2.69 for the GMCs, and 0.86 for the clumps and cores, suggesting the decrease of the virial parameter from large-scale GMCs

to smaller-scale clumps and cores. The surface density increases from giant molecular clouds to dense cores, with a median value of surface density being 0.04 g cm^{-2} for the GMCs in contrast to 0.38 g cm^{-2} for the clumps and cores. To conclude, the different behaviors between these two types of density structures in the \mathcal{L} distribution suggest a dynamical decoupling between the large-scale clouds and the smaller-scale clumps/cores, which agrees with the finding of Peretto et al. (2023).

4. DISCUSSION

4.1. Relation of cloud dynamics to turbulence, gravity, and magnetic field

Turbulence is ubiquitous in molecular clouds. The turbulence on large scale can be driven by various sources such as cloud-cloud collisions, supernova explosions, and the expansion of HII regions (e.g., Ostriker & Shetty 2011; Inoue

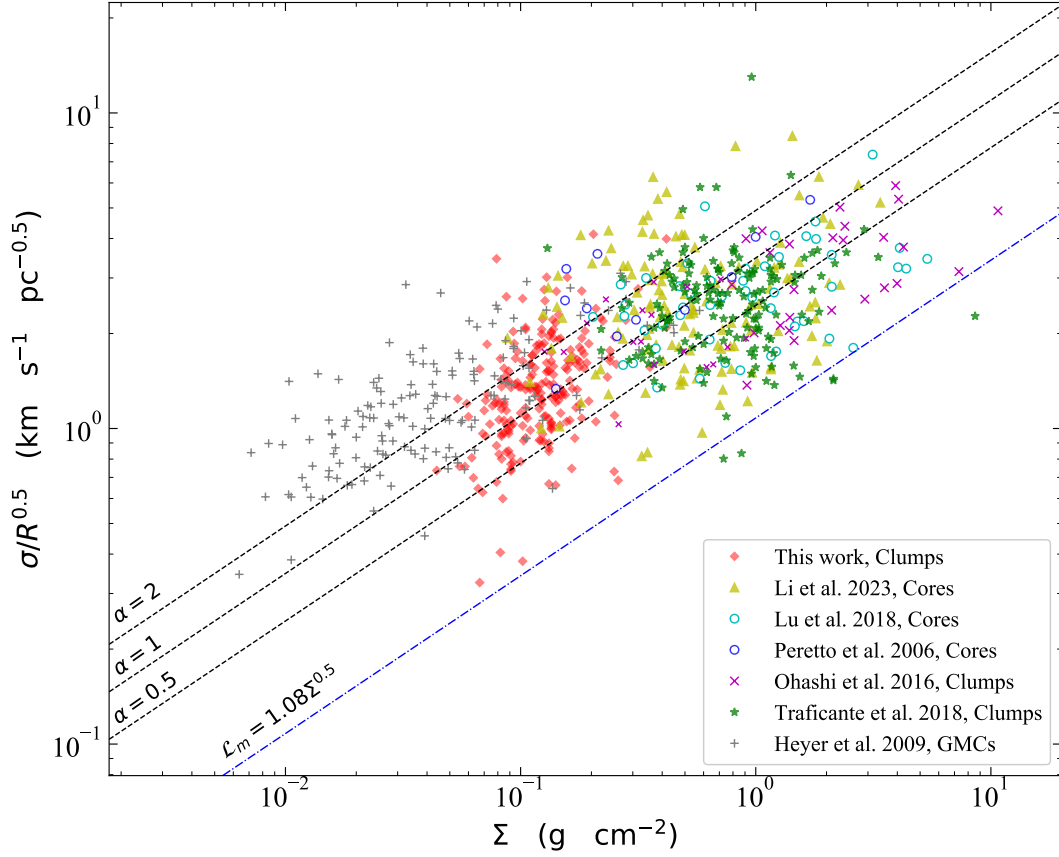


Figure 6. \mathcal{L} – Σ relation for different density structures from GMCs to dense cores, where \mathcal{L} is the $\sigma/R^{0.5}$ ratio. The black dashed lines correspond to different predicted \mathcal{L} – Σ relation at the virial parameters of 0.5, 1, and 2. The dash-dotted line indicates the predicted, magnetic version of the \mathcal{L} – Σ relation, $\mathcal{L}_m = 1.08 \Sigma^{0.5}$, which corresponds to a simple model of magnetically supported clouds in an equilibrium state.

& Fukui 2013b). As shown in Fig. 5, strong turbulent motions appear in the large-scale MCs, as reflected in the high velocity dispersion at scales of ~ 10 pc. This implies that turbulence would have a relatively stronger effect on the large-scale dynamics of molecular clouds and thus delay their gravity collapse. Nevertheless, the turbulence cascades toward small scales in MCs, resulting in turbulence gradually becoming less important. Notably, in small-scale dense cores with a size of ~ 0.01 pc, the gas velocity dispersion sharply decreases. This implies that if there are no internal, localized driving sources to maintain it, turbulence will quickly dissipate in dense cores.

In order to further investigate the interaction between turbulence and gravity, we conducted a more detailed analysis of the GMC sample from Heyer et al. (2009). We divided the sample into low surface density sub-samples, which contained 129 sources ($\Sigma < 0.1 \text{ g cm}^{-2}$), and high surface density sub-samples, containing 29 sources ($\Sigma \geq 0.1 \text{ g cm}^{-2}$).

The difference in median surface density between two sub-samples is about five factor, with values of 0.03 g cm^{-2} and 0.16 g cm^{-2} , respectively. As shown in Figure 7, an observed trend indicates that as the surface density increases, the size of clouds correspondingly decreases, reflecting cloud contraction. Furthermore, the evolution from an over-virial state to a sub-virial state during cloud contraction suggests that gravity becomes relatively more important compared to turbulence. In addition, although the turbulence dissipates during cloud contraction, the variation in velocity dispersion of MCs is not significant, indicating that the gravitational contraction contributes to non-thermal motions but not significantly. Such gravity-driven non-thermal motions are plausible on large-scale MCs, as several analysis of the column density distribution function of large-scale clouds have indicated signs of global collapse (e.g., Schneider et al. 2013, 2015).

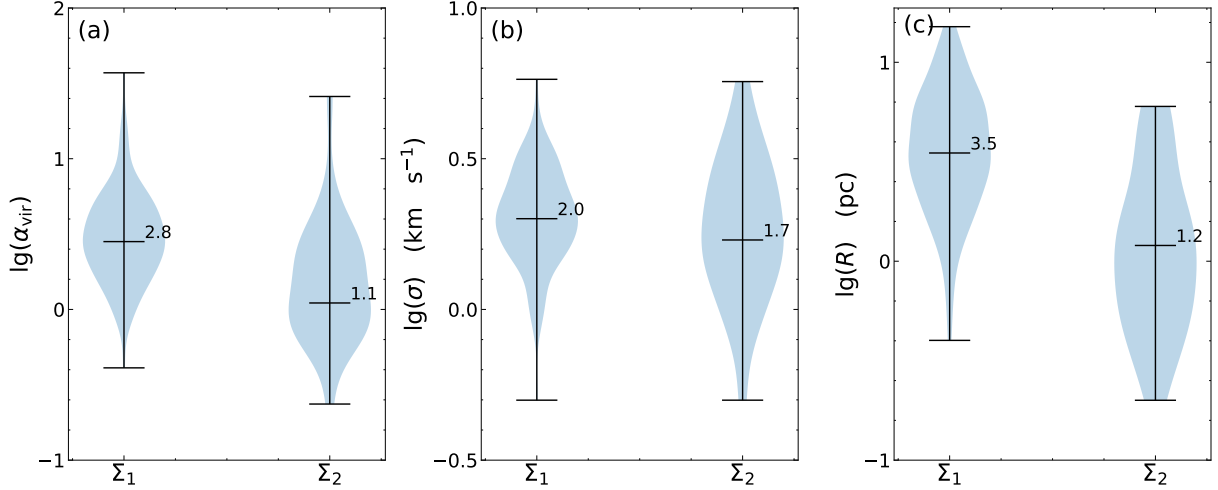


Figure 7. Violin plot of the α_{vir} , velocity dispersion, and size distribution for the GMCs in two sub-samples with different mass surface density. The shape of each distribution shows the probability density of the α_{vir} , velocity dispersion, and size, respectively. The black horizontal bars from the top to bottom in violin plot represent the maximum, median, and minimum values, respectively. The Σ_1 on the horizontal axis represents the median of sub-samples with low mass surface density, while Σ_2 represents the median of sub-samples with high mass surface density, which are 0.03 g cm^{-2} and 0.16 g cm^{-2} , respectively.

We can further explore how turbulence and gravity affect the cloud dynamics by scrutinizing the observed \mathcal{L} - Σ relation in Figure 6 from left to right. The relation shows that clouds change from an over-virial state (i.e., $\alpha_{\text{vir}} > 2$ for the majority of large-scale clouds) to a sub-virial state ($\alpha_{\text{vir}} < 2$ for most smaller-scale density structures) as they become smaller and denser, which is also evident in the distribution of the virial parameter across density scales in Figure 8. This observed transition suggests that the effect of turbulence on the dynamics of clouds could gradually weaken during their evolution, while the effect of gravity gradually strengthen. This finding is consistent with the results of Peretto et al. (2023), who found that small-scale, dense density structures up to filaments are governed by gravity over turbulence by performing systematical, multiscale analysis of the virial parameter and velocity dispersion of 27 filamentary clouds. Moreover, the simulation of dense core collapse suggests that turbulence does not have a significant impact on the dynamics of dense cores if it is dissipated promptly after being generated (Guerrero-Gamboa & Vázquez-Semadeni 2020).

Therefore, we suggest that both turbulence and gravity could play crucial roles in regulating together the dynamics of molecular clouds. The ubiquitous turbulence would impact profoundly the dynamics of large-scale MCs before they become sub-virial; subsequently, the self-gravity in sub-virial MCs becomes important down to core scales, leading to global hierarchical collapse as proposed in Vázquez-Semadeni et al. 2019.

It is worth noting that large-scale clouds are generally observed to transition from an over-virial state to a sub-virial state (see Fig. 7), subsequently fragmenting hierarchically

into smaller, sub-virial density structures such as cores and clumps. This fragmentation aligns with the GHC model, where gravity dominates the collapse of molecular clouds (Hartmann et al. 2001; Ballesteros-Paredes et al. 2011a, 2018; Vázquez-Semadeni et al. 2019). Interestingly, some smaller structures, especially at the core and clump scales, appear to be in an over-virial state (Fig. 5). As predicted in the GHC model, the velocity dispersion in these structures could be amplified by non-thermal motions induced by cloud collapse. These motions, being a result of an ordered collapse process, could be more structured than random turbulence, leading to a pseudo over-virial state. On the other hand, these particular small-scale structures could be really over-virial if they are subjected to strong local stellar feedback, such as outflows and stellar winds (Pan et al. 2024).

Strong magnetic fields in MCs can counteract the effects of turbulence and gravity, as evidenced by the ordered appearance of field morphology from thermal dust emission polarization (e.g., Li et al. 2013; Planck Collaboration et al. 2016; Soler et al. 2016; Gu & Li 2019). In the presence of strong magnetic fields, cloud motions become sub-Alfvénic, meaning that neutral gas is dynamically coupled to the field through ion-neutral collisions. These cloud motions may originate from the propagation of large amplitude, long wavelength Alfvén waves (Heyer et al. 2009). Mouschovias et al. (2006) proposed a simple model of magnetically supported clouds that can reach an equilibrium state when the cloud surface density equals the magnetic critical surface density, given by the equation $\Sigma_{\text{crit,m}} = B/(63G)^{1/2}$. If the magnetic field strength can be predicted from the observed σ^2/R ratio using the equation $B \sim (45/G)^{1/2} \sigma^2/R$,

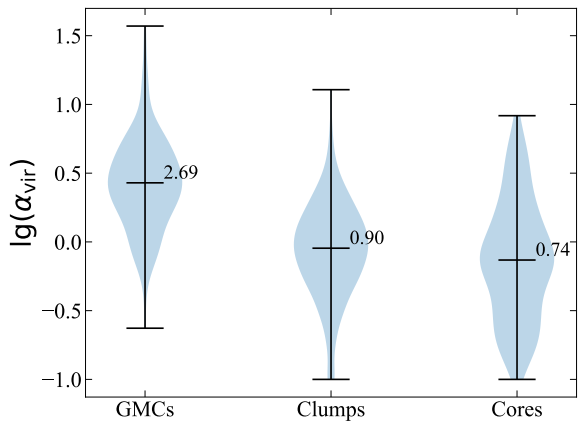


Figure 8. Violin plot of the α_{vir} distribution for different density structures. The shape of each distribution shows the probability density of the α_{vir} . The black horizontal bars from the top to bottom in violin plot represent the maximum, median, and minimum values, respectively. For different density structures, the median values of the α_{vir} are 2.69, 0.90, and 0.74, respectively. The data for GMCs is sourced from Heyer et al. (2009). The data for clumps are from Ohashi et al. (2016), Traficante et al. (2018), and this work, respectively. The data for cores are from Peretto et al. (2006), Ohashi et al. (2016), Lu et al. (2018), and Li et al. (2023), respectively.

as demonstrated by Myers & Goodman (1988) for several nearby clouds with thermal Zeeman OH measurements, then magnetically supported clouds in equilibrium will satisfy the magnetic version of the $\mathcal{L}-\Sigma$ relation, $\mathcal{L}_m = 1.08 \Sigma^{0.5}$. Figure 6 shows that the predicted $\mathcal{L}_m-\Sigma$ relation is much lower than the observed data points. This suggests that the magnetic fields alone may not be sufficient to maintain cloud against cloud gravitational collapse (e.g., Traficante et al. 2018). Nevertheless, magnetic fields may still have a crucial role in other aspects of cloud dynamics, such as filament formation and protostellar disk support. To fully understand the role of magnetic fields in cloud’s dynamics, we require a comprehensive approach that accounts for the complex interplay between turbulence, gravity, and magnetic fields on different scales.

It is important to note that the discussions we made above on the $\sigma-R$ and $\mathcal{L}-\Sigma$ relations may be affected by observational biases, as the data were obtained using different telescopes, molecular tracers and analysis techniques. In addition, one must recognise that systematics from different surveys may influence current analysis. For example, we excluded the CO cloud data from Roman-Duval et al. (2010), who gathered data from both the University of Massachusetts-Stony Brook (UMSB) and Galactic Ring surveys. Our data from Heyer et al. (2009), however, solely originate from the latter. The Roman-Duval’s data, leading to

virial parameters averaging six times lower than Heyer’s (as depicted in Fig. 1 of Kauffmann et al. (2013)), does not conform to the trend shown in Fig. 8. Besides, different molecular tracers can have different physical properties and trace different density regions. Therefore, for more robust discussions on the $\sigma-R$ and $\mathcal{L}-\Sigma$ relations, we require in the future consistent, multiscale kinematic observations of molecular clouds using the same telescope and molecular tracer as much as possible.

4.2. Implication on high-mass star formation

As discussed earlier, the $\sigma-R$ relation could provide insight into the role of turbulence and gravity in molecular cloud dynamics. This would allow us from a global view to place a constraint on the latest theoretical models of high-mass star formation, such as GHC and I2. Both models suggest that high-mass star formation in molecular clouds is a multiscale process involving fragmentation and mass accretion at various density scales. The strong correlation observed in the $\sigma-R$ relation supports the kinematic connection between different density structures from clouds to cores, and thus the multiscale nature of high-mass star formation.

Mass accretion is one of the key multiscale physical processes. Both GHC and I2 models agree that gravity drives mass accretion on small scales, such as cores/clumps and even filaments. However, they differ in their predictions for larger scales. That is, the GHC model posits that gravity primarily drives hierarchical mass accretion across all density scales of a cloud (Vázquez-Semadeni et al. 2019). Conversely, the I2 model proposes that turbulence regulates mass inflow and accretion on large-scale clouds (Padoan et al. 2020), with the self-gravity of the clouds assuming control at smaller density scales. As discussed in Sect. 4.1, the $\sigma-R$ and $\mathcal{L}-\Sigma$ relations we observed indicate that both turbulence and gravity can control the dynamics of MCs, with the former possibly dominating in large-scale over-virial state clouds and the latter dominating in sub-virial density structures including large-scale clouds down to smaller-scale clumps and cores. This finding implies that the GHC model effectively accounts for high-mass star formation in sub-virial clouds, which form smaller hierarchical density structures due to gravitational instability. However, our analysis also argues that the role of turbulence may not be overlooked until large-scale clouds reach a sub-virial state. This argument is consistent with the finding of the ubiquitous filamentary density structures in HI clouds where the self-gravity of clouds is not as important as turbulence (e.g., Holm-Hansen et al. 2023; Liu et al. 2024).

5. CONCLUSIONS

We have investigated the implication of the velocity dispersion scalings on high-mass star formation in molecular

clouds, including the scalings of Larson’s linewidth–size (σ – R) and Larson’s ratio–mass surface density (\mathcal{L} – Σ ; here $\mathcal{L} = \sigma/R^{0.5}$). Our investigations were based on systematic analysis of the σ parameter of well-selected 221 massive clumps, complemented with published samples of other hierarchical density structures of molecular clouds over spatial scales of 0.01–10 pc. Our investigations would allow to put a constraint to theoretical models of multiscale, dynamical high-mass star formation. Our major results can be summarized as follows:

- The high median value of mass surface density of $> 0.05 \text{ g cm}^{-2}$ indicates that the majority of the 221 massive clumps are most likely to form high-mass stars. Based on the IR signatures between 3.6 and $24 \mu\text{m}$, these clumps are classified into four evolutionary phases, including 18 quiescent, 100 protostellar, 84 HII region, and 19 PDR clumps.
- The velocity dispersion (σ) of the clumps increases with the evolutionary sequence from the quiescent to HII region phase, which is related to enhanced stellar feedback in more evolved phases. Then, the σ distribution decreases toward the PDR clumps, but is still higher than in the quiescent and protostellar phases. This could be because PDRs are less influenced by stellar feedback than HII regions.
- In the relation of Larson’s linewidth–size (σ – R) for our sample alone, we find a weak correlation (the Pearson’s correlation coefficient $\rho = 0.43$) due to the limited range of spatial scales of the sample. In the relation of Larson’s ratio–mass surface density (\mathcal{L} – Σ), we find the same result ($\rho = 0.42$) but due to the limited range of the mass surface density of the sample.
- Both the σ – R and \mathcal{L} – Σ relations show strong correlations ($\rho > 0.75$) when combining our sample with other density structures collected from the literature, including molecular clouds, massive clumps, and massive cores.

- In the σ – R relation, the strong correlation suggests that if turbulence is important in regulating the dynamics of cloud structures, the turbulent motions will cascade with a decreasing scale.
- In the \mathcal{L} – Σ relation, clouds transition from over-virial state ($\alpha_{\text{vir}} > 2$) to sub-virial state ($\alpha_{\text{vir}} < 2$) as they become smaller and denser. This could reflect a shift in the governing force from turbulence to gravity.

The results inferred from both σ – R and \mathcal{L} – Σ relations for different density structures from large-scale MCs to smaller-scale filaments, clumps, and dense cores, suggest that both turbulence and gravity could be important in regulating together the dynamics of hierarchical density structures of molecular clouds, with turbulence possibly prevailing in large-scale over-virial state clouds and gravity prevailing in sub-virial state clouds and smaller-scale hierarchical density structures such as clumps and cores. We suggest that the multiscale physical process of high-mass star formation hinges on the self-gravity of sub-virial molecular clouds (MCs). This perspective aligns with the framework of the GHC model proposed by [Vázquez-Semadeni et al. \(2019\)](#). However, we emphasize that the influence of turbulence may not be dismissed until large-scale clouds attain a sub-virial state, which is yet to be confirmed by future multiscale kinematic observations of molecular clouds using the same telescope and molecular tracer as much as possible.

We thank the anonymous referee for comments and suggestions that greatly improved the quality of this paper. This work has been supported by the National Key R&D Program of China (No. 2022YFA1603101). H.-L. Liu is supported by National Natural Science Foundation of China (NSFC) through the grant No. 12103045, and , and by Yunnan Fundamental Research Project (grant No. 202301AT070118, 202401AS070121). S.-L. Qin is supported by NSFC under No. 12033005.

APPENDIX

A. EXAMPLES OF CLASSIFICATION

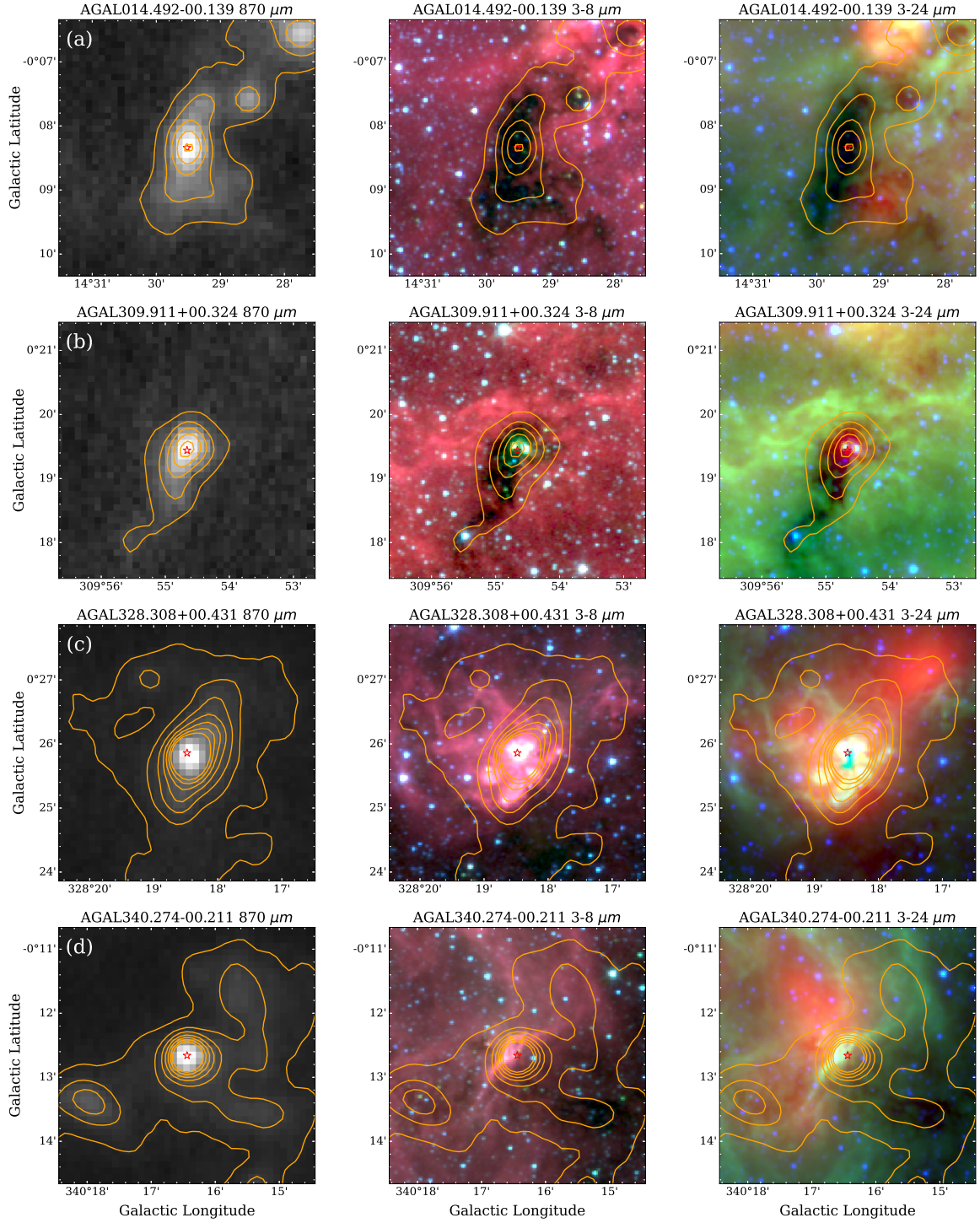


Figure 9. An example of clump classification inferred from *Spitzer* images overlaid with 870 μm dust continuum emission. In each row from left to right, the images are ATLASGAL 870 μm dust continuum emission in grey-scale, *Spitzer* three-colour image of 3.6, 4.5 and 8.0 μm , and *Spitzer* three-colour image of 3.6, 8.0 and 24 μm . the yellow contours indicate the 870 μm dust continuum emission, starting from 0.3 Jy/beam with a step of 0.5 Jy/beam. Rows (a)–(d) correspond to the examples of classified phases of clumps from the quiescent, protostellar, HII region, and PDR phase, respectively. In all images, the clump name is indicated at the top of each panel. The red star symbol identifies peak emission at 870 μm of the clump.

B. PHYSICAL PROPERTIES OF CLUMPS

Table 1. Physical properties of clumps

ID	Sname	l	b	R	Σ	M	L	σ	α_{vir}	evol.phase
		deg	deg	pc	g cm^{-2}	M_{\odot}	L_{\odot}	km s^{-1}		
1	AGAL010.168-00.362	10.168	-0.362	0.86 ± 0.17	0.08 ± 0.01	883 ± 260	231739	3.2 ± 0.14	11.65 ± 4.43	HII region
2	AGAL010.204-00.347	10.204	-0.347	0.68 ± 0.14	0.18 ± 0.01	1263 ± 380	29376	1.46 ± 0.1	1.33 ± 0.5	PDR
3	AGAL010.213-00.322	10.213	-0.322	1.11 ± 0.22	0.14 ± 0.02	2684 ± 810	40272	2.42 ± 0.13	2.8 ± 1.07	Protostellar
4	AGAL010.228-00.207	10.228	-0.207	1.0 ± 0.2	0.13 ± 0.01	1968 ± 590	2979	0.84 ± 0.09	0.42 ± 0.16	Protostellar
5	AGAL010.299-00.147	10.299	-0.147	0.93 ± 0.19	0.13 ± 0.01	1622 ± 490	98628	2.65 ± 0.18	4.65 ± 1.77	HII region
6	AGAL010.323-00.161	10.323	-0.161	0.98 ± 0.2	0.1 ± 0.01	1465 ± 440	179473	1.62 ± 0.14	2.03 ± 0.77	HII region
7	AGAL010.342-00.142	10.342	-0.142	0.59 ± 0.12	0.13 ± 0.01	690 ± 210	11695	1.17 ± 0.15	1.38 ± 0.52	Protostellar
8	AGAL010.472+00.027	10.472	0.027	3.07 ± 0.61	0.13 ± 0.01	18340 ± 5500	442588	2.65 ± 0.21	1.37 ± 0.52	HII region
9	AGAL010.624-00.384	10.624	-0.384	1.47 ± 0.29	0.1 ± 0.01	3100 ± 930	323594	2.02 ± 0.13	2.26 ± 0.86	Protostellar
10	AGAL010.626-00.337	10.626	-0.337	1.07 ± 0.21	0.12 ± 0.02	2067 ± 620	20559	1.05 ± 0.09	0.67 ± 0.25	HII region
11	AGAL010.972-00.094	10.972	-0.094	0.77 ± 0.15	0.14 ± 0.01	1255 ± 380	253	0.58 ± 0.07	0.24 ± 0.09	Protostellar
12	AGAL011.064-00.099	11.064	-0.099	0.85 ± 0.17	0.16 ± 0.01	1797 ± 540	402	0.69 ± 0.11	0.26 ± 0.1	Quiescent
13	AGAL011.109-00.397	11.109	-0.397	0.39 ± 0.08	0.12 ± 0.01	288 ± 90	2000	1.39 ± 0.13	3.08 ± 1.17	HII region
14	AGAL011.126-00.127	11.126	-0.127	1.09 ± 0.22	0.25 ± 0.02	4464 ± 1340	815	1.15 ± 0.09	0.37 ± 0.14	Protostellar
15	AGAL011.344+00.796	11.344	0.796	0.43 ± 0.09	0.1 ± 0.02	287 ± 90	95	0.61 ± 0.1	0.64 ± 0.24	Protostellar
16	AGAL011.917-00.612	11.917	-0.612	1.0 ± 0.2	0.18 ± 0.02	2654 ± 800	16827	1.63 ± 0.11	1.15 ± 0.44	Protostellar
17	AGAL011.936-00.616	11.936	-0.616	1.01 ± 0.2	0.14 ± 0.01	2127 ± 640	57412	1.95 ± 0.16	2.1 ± 0.8	HII region
18	AGAL012.418+00.506	12.418	0.506	0.56 ± 0.11	0.09 ± 0.01	414 ± 120	7889	1.05 ± 0.04	1.74 ± 0.66	HII region
19	AGAL012.496-00.222	12.496	-0.222	0.51 ± 0.1	0.1 ± 0.01	386 ± 120	158	0.8 ± 0.07	0.97 ± 0.37	Protostellar
20	AGAL012.776-00.211	12.776	-0.211	0.53 ± 0.11	0.11 ± 0.01	462 ± 140	3162	1.16 ± 0.05	1.78 ± 0.68	Quiescent
21	AGAL012.804-00.199	12.804	-0.199	1.37 ± 0.27	0.14 ± 0.03	3890 ± 1170	125893	1.84 ± 0.04	1.39 ± 0.53	HII region
22	AGAL012.853-00.226	12.853	-0.226	0.73 ± 0.15	0.11 ± 0.03	881 ± 260	5140	1.14 ± 0.06	1.25 ± 0.47	PDR
23	AGAL012.856-00.209	12.856	-0.209	0.42 ± 0.08	0.09 ± 0.01	255 ± 80	841	1.21 ± 0.12	2.84 ± 1.08	Quiescent
24	AGAL012.863-00.244	12.863	-0.244	0.73 ± 0.15	0.1 ± 0.02	841 ± 250	...	0.94 ± 0.06	0.89 ± 0.34	PDR
25	AGAL012.888+00.489	12.888	0.489	0.86 ± 0.17	0.11 ± 0.03	1234 ± 370	17947	1.58 ± 0.13	2.01 ± 0.76	HII region
26	AGAL012.908-00.259	12.908	-0.259	1.04 ± 0.21	0.2 ± 0.02	3195 ± 960	39719	1.9 ± 0.12	1.37 ± 0.52	Protostellar
27	AGAL013.209-00.144	13.209	-0.144	3.72 ± 0.74	0.1 ± 0.02	20851 ± 6260	323594	1.52 ± 0.12	0.48 ± 0.18	HII region
28	AGAL013.213+00.039	13.213	0.039	1.04 ± 0.21	0.14 ± 0.01	2180 ± 650	...	1.01 ± 0.08	0.57 ± 0.21	PDR
29	AGAL013.243-00.086	13.243	-0.086	0.66 ± 0.13	0.24 ± 0.01	1587 ± 480	356	1.44 ± 0.1	1.01 ± 0.38	Protostellar
30	AGAL013.276-00.334	13.276	-0.334	0.79 ± 0.16	0.16 ± 0.01	1532 ± 460	412	0.95 ± 0.07	0.54 ± 0.2	Protostellar
31	AGAL013.902-00.516	13.902	-0.516	0.39 ± 0.08	0.09 ± 0.02	210 ± 60	93	0.64 ± 0.09	0.88 ± 0.33	Protostellar
32	AGAL014.011-00.176	14.011	-0.176	0.55 ± 0.11	0.11 ± 0.02	493 ± 150	1462	1.07 ± 0.11	1.48 ± 0.56	Protostellar
33	AGAL014.084-00.554	14.084	-0.554	0.41 ± 0.08	0.09 ± 0.02	224 ± 70	228	0.73 ± 0.06	1.16 ± 0.44	Quiescent
34	AGAL014.114-00.574	14.114	-0.574	0.58 ± 0.12	0.14 ± 0.02	714 ± 210	793	1.65 ± 0.12	2.57 ± 0.98	Protostellar
35	AGAL014.181-00.529	14.181	-0.529	0.35 ± 0.07	0.12 ± 0.01	218 ± 70	137	0.76 ± 0.05	1.08 ± 0.41	Quiescent
36	AGAL014.194-00.194	14.194	-0.194	1.23 ± 0.25	0.15 ± 0.0	3442 ± 1030	3724	1.42 ± 0.1	0.83 ± 0.32	Protostellar
37	AGAL014.197-00.509	14.197	-0.509	0.39 ± 0.08	0.13 ± 0.02	298 ± 90	596	0.54 ± 0.04	0.44 ± 0.17	Quiescent
38	AGAL014.227-00.511	14.227	-0.511	0.56 ± 0.11	0.14 ± 0.02	643 ± 190	1531	0.78 ± 0.05	0.62 ± 0.23	Protostellar
39	AGAL014.331-00.644	14.331	-0.644	0.59 ± 0.12	0.14 ± 0.01	757 ± 230	5848	1.47 ± 0.04	1.96 ± 0.74	Protostellar
40	AGAL014.492-00.139	14.492	-0.139	1.09 ± 0.22	0.18 ± 0.02	3206 ± 960	3420	1.64 ± 0.14	1.07 ± 0.41	Quiescent
41	AGAL014.621-00.579	14.621	-0.579	0.17 ± 0.03	0.18 ± 0.02	77 ± 20	173	0.79 ± 0.08	1.59 ± 0.6	Protostellar
42	AGAL014.626-00.562	14.626	-0.562	0.45 ± 0.09	0.14 ± 0.01	443 ± 130	...	0.82 ± 0.05	0.8 ± 0.3	Quiescent

Table 1 continued

Table 1 (continued)

ID	Sname	l	b	R	Σ	M	L	σ	α_{vir}	evol.phase
		deg	deg	pc	g cm^{-2}	M_{\odot}	L_{\odot}	km s^{-1}		
43	AGAL014.632-00.577	14.632	-0.577	0.45 ± 0.09	0.14 ± 0.02	431 ± 130	1690	0.85 ± 0.05	0.87 ± 0.33	Protostellar
44	AGAL018.888-00.474	18.888	-0.474	1.52 ± 0.3	0.09 ± 0.02	3181 ± 950	34995	1.66 ± 0.12	1.54 ± 0.59	Protostellar
45	AGAL300.951+00.894	300.951	0.894	0.54 ± 0.11	0.08 ± 0.02	378 ± 110	1043	0.88 ± 0.09	1.28 ± 0.49	Quiescent
46	AGAL301.136-00.226	301.136	-0.226	1.15 ± 0.23	0.12 ± 0.02	2450 ± 740	71410	1.32 ± 0.12	0.95 ± 0.36	Protostellar
47	AGAL302.391+00.281	302.391	0.281	1.21 ± 0.24	0.07 ± 0.01	1566 ± 470	7364	1.35 ± 0.13	1.64 ± 0.62	HII region
48	AGAL305.197+00.007	305.197	0.007	0.83 ± 0.17	0.12 ± 0.01	1275 ± 380	27605	1.88 ± 0.16	2.67 ± 1.01	HII region
49	AGAL305.226+00.274	305.226	0.274	1.05 ± 0.21	0.19 ± 0.02	3198 ± 960	39082	1.66 ± 0.13	1.05 ± 0.4	Protostellar
50	AGAL305.271-00.009	305.271	-0.009	1.36 ± 0.27	0.12 ± 0.01	3327 ± 1000	168773	1.35 ± 0.14	0.86 ± 0.33	HII region
51	AGAL308.124-00.334	308.124	-0.334	0.83 ± 0.17	0.09 ± 0.02	939 ± 280	463	0.96 ± 0.13	0.95 ± 0.36	Protostellar
52	AGAL309.236-00.457	309.236	-0.457	0.71 ± 0.14	0.08 ± 0.01	607 ± 180	1308	1.01 ± 0.1	1.37 ± 0.52	Protostellar
53	AGAL309.421-00.621	309.421	-0.621	0.91 ± 0.18	0.12 ± 0.02	1482 ± 440	2123	0.87 ± 0.09	0.54 ± 0.21	Protostellar
54	AGAL309.534-00.741	309.534	-0.741	1.45 ± 0.29	0.11 ± 0.03	3463 ± 1040	20274	1.19 ± 0.11	0.69 ± 0.26	PDR
55	AGAL309.911+00.324	309.911	0.324	1.24 ± 0.25	0.14 ± 0.01	3102 ± 930	2996	1.12 ± 0.11	0.58 ± 0.22	Protostellar
56	AGAL310.014+00.387	310.014	0.387	0.82 ± 0.16	0.09 ± 0.01	885 ± 270	11448	0.9 ± 0.05	0.87 ± 0.33	HII region
57	AGAL310.144+00.759	310.144	0.759	1.09 ± 0.22	0.09 ± 0.02	1651 ± 500	14656	0.81 ± 0.06	0.51 ± 0.19	HII region
58	AGAL311.044+00.687	311.044	0.687	0.45 ± 0.09	0.08 ± 0.02	241 ± 70	775	0.59 ± 0.07	0.76 ± 0.29	Protostellar
59	AGAL311.512-00.454	311.512	-0.454	0.57 ± 0.11	0.08 ± 0.02	410 ± 120	8585	1.08 ± 0.13	1.9 ± 0.72	Protostellar
60	AGAL311.567+00.319	311.567	0.319	0.55 ± 0.11	0.18 ± 0.02	842 ± 250	2458	2.03 ± 0.18	3.16 ± 1.2	Protostellar
61	AGAL311.979-00.954	311.979	-0.954	0.39 ± 0.08	0.1 ± 0.02	240 ± 70	570	0.86 ± 0.08	1.39 ± 0.53	Protostellar
62	AGAL312.108+00.309	312.108	0.309	0.82 ± 0.16	0.08 ± 0.01	851 ± 260	75812	1.4 ± 0.13	2.19 ± 0.83	HII region
63	AGAL313.766-00.862	313.766	-0.862	0.81 ± 0.16	0.12 ± 0.02	1202 ± 360	6348	1.79 ± 0.12	2.49 ± 0.95	HII region
64	AGAL314.219+00.271	314.219	0.271	1.83 ± 0.37	0.14 ± 0.01	6826 ± 2050	48857	1.42 ± 0.11	0.63 ± 0.24	Protostellar
65	AGAL314.319+00.111	314.319	0.111	0.89 ± 0.18	0.12 ± 0.03	1371 ± 410	8690	1.47 ± 0.12	1.63 ± 0.62	HII region
66	AGAL316.752-00.012	316.752	-0.012	0.72 ± 0.14	0.18 ± 0.04	1393 ± 420	214688	1.54 ± 0.07	1.43 ± 0.54	PDR
67	AGAL316.764-00.012	316.764	-0.012	0.3 ± 0.06	0.32 ± 0.03	416 ± 120	3626	1.51 ± 0.08	1.88 ± 0.71	Protostellar
68	AGAL316.769-00.002	316.769	-0.002	0.35 ± 0.07	0.13 ± 0.04	232 ± 70	8997	1.77 ± 0.12	5.45 ± 2.07	Quiescent
69	AGAL316.799-00.056	316.799	-0.056	0.67 ± 0.13	0.16 ± 0.01	1064 ± 320	18001	2.46 ± 0.12	4.44 ± 1.69	HII region
70	AGAL316.811-00.059	316.811	-0.059	0.73 ± 0.15	0.14 ± 0.0	1141 ± 340	34453	2.33 ± 0.11	4.03 ± 1.53	HII region
71	AGAL317.701+00.109	317.701	0.109	1.16 ± 0.23	0.13 ± 0.02	2656 ± 800	4200	0.97 ± 0.09	0.47 ± 0.18	HII region
72	AGAL317.867-00.151	317.867	-0.151	0.47 ± 0.09	0.13 ± 0.01	419 ± 130	925	1.74 ± 0.2	3.93 ± 1.49	Protostellar
73	AGAL317.879-00.254	317.879	-0.254	0.4 ± 0.08	0.2 ± 0.02	489 ± 150	476	2.61 ± 0.21	6.46 ± 2.45	Protostellar
74	AGAL318.049+00.086	318.049	0.086	0.86 ± 0.17	0.1 ± 0.01	1171 ± 350	26792	1.23 ± 0.09	1.3 ± 0.49	HII region
75	AGAL318.783-00.174	318.783	-0.174	0.37 ± 0.07	0.1 ± 0.01	214 ± 60	1665	0.71 ± 0.09	1.0 ± 0.38	Protostellar
76	AGAL318.948-00.197	318.948	-0.197	0.43 ± 0.09	0.17 ± 0.02	470 ± 140	43113	1.12 ± 0.06	1.34 ± 0.51	HII region
77	AGAL320.169+00.824	320.169	0.824	1.01 ± 0.2	0.09 ± 0.01	1393 ± 420	30783	0.74 ± 0.07	0.46 ± 0.17	PDR
78	AGAL320.247+00.404	320.247	0.404	0.75 ± 0.15	0.07 ± 0.01	622 ± 190	7902	0.89 ± 0.09	1.11 ± 0.42	Protostellar
79	AGAL320.891-00.412	320.891	-0.412	0.63 ± 0.13	0.11 ± 0.01	659 ± 200	36186	1.27 ± 0.13	1.8 ± 0.68	Protostellar
80	AGAL321.703+01.171	321.703	1.171	0.54 ± 0.11	0.14 ± 0.01	602 ± 180	1889	1.5 ± 0.1	2.35 ± 0.89	Protostellar
81	AGAL321.719+01.176	321.719	1.176	0.79 ± 0.16	0.13 ± 0.01	1218 ± 370	195813	1.44 ± 0.11	1.56 ± 0.59	HII region
82	AGAL321.904-00.016	321.904	-0.016	0.49 ± 0.1	0.07 ± 0.01	243 ± 70	514	1.08 ± 0.12	2.75 ± 1.04	Quiescent
83	AGAL321.934-00.006	321.934	-0.006	0.52 ± 0.1	0.12 ± 0.01	498 ± 150	2518	0.93 ± 0.09	1.06 ± 0.4	Protostellar
84	AGAL322.158+00.636	322.158	0.636	1.47 ± 0.29	0.12 ± 0.02	3974 ± 1190	161295	2.22 ± 0.16	2.12 ± 0.8	HII region
85	AGAL322.164+00.622	322.164	0.622	0.91 ± 0.18	0.14 ± 0.02	1702 ± 510	72948	1.96 ± 0.12	2.39 ± 0.91	HII region
86	AGAL322.521+00.636	322.521	0.636	0.63 ± 0.13	0.09 ± 0.01	561 ± 170	1009	0.82 ± 0.08	0.89 ± 0.34	Protostellar
87	AGAL323.727-00.279	323.727	-0.279	0.78 ± 0.16	0.15 ± 0.0	1349 ± 400	1871	0.9 ± 0.09	0.55 ± 0.21	Quiescent
88	AGAL323.741-00.264	323.741	-0.264	0.85 ± 0.17	0.12 ± 0.01	1355 ± 410	15117	0.89 ± 0.1	0.57 ± 0.22	HII region

Table 1 continued

Table 1 (continued)

ID	Sname	l	b	R	Σ	M	L	σ	α_{vir}	evol.phase
		deg	deg	pc	g cm^{-2}	M_{\odot}	L_{\odot}	km s^{-1}		
89	AGAL324.923-00.569	324.923	-0.569	1.21 ± 0.24	0.08 ± 0.02	1717 ± 510	19612	1.32 ± 0.14	1.43 ± 0.55	HII region
90	AGAL326.472-00.377	326.472	-0.377	0.92 ± 0.18	0.08 ± 0.01	1053 ± 320	18097	1.1 ± 0.14	1.23 ± 0.47	HII region
91	AGAL326.474+00.702	326.474	0.702	0.62 ± 0.12	0.14 ± 0.01	828 ± 250	157146	0.96 ± 0.07	0.8 ± 0.31	Protostellar
92	AGAL326.607+00.799	326.607	0.799	0.5 ± 0.1	0.14 ± 0.01	510 ± 150	557	1.42 ± 0.13	2.3 ± 0.88	Protostellar
93	AGAL326.627+00.611	326.627	0.611	0.68 ± 0.14	0.26 ± 0.0	1773 ± 530	17441	1.32 ± 0.07	0.77 ± 0.29	Protostellar
94	AGAL326.641+00.612	326.641	0.612	0.61 ± 0.12	0.42 ± 0.01	2321 ± 700	15582	1.63 ± 0.06	0.81 ± 0.31	PDR
95	AGAL326.647+00.749	326.647	0.749	0.51 ± 0.1	0.09 ± 0.02	335 ± 100	854	1.0 ± 0.1	1.75 ± 0.66	Protostellar
96	AGAL326.652+00.619	326.652	0.619	0.2 ± 0.04	0.42 ± 0.02	246 ± 70	2683	1.78 ± 0.09	2.95 ± 1.12	PDR
97	AGAL326.657+00.594	326.657	0.594	0.65 ± 0.13	0.13 ± 0.02	803 ± 240	95796	1.5 ± 0.07	2.13 ± 0.81	HII region
98	AGAL326.724+00.614	326.724	0.614	0.53 ± 0.11	0.1 ± 0.0	442 ± 130	29886	1.52 ± 0.12	3.21 ± 1.22	HII region
99	AGAL327.273-00.574	327.273	-0.574	0.63 ± 0.13	0.14 ± 0.01	802 ± 240	6673	1.38 ± 0.12	1.74 ± 0.66	HII region
100	AGAL327.293-00.579	327.293	-0.579	1.2 ± 0.24	0.24 ± 0.01	5236 ± 1570	104289	1.84 ± 0.07	0.91 ± 0.35	HII region
101	AGAL327.301-00.552	327.301	-0.552	1.18 ± 0.24	0.1 ± 0.01	2203 ± 660	557269	2.24 ± 0.1	3.12 ± 1.19	HII region
102	AGAL327.711-00.396	327.711	-0.396	0.78 ± 0.16	0.13 ± 0.01	1217 ± 370	1116	1.21 ± 0.09	1.1 ± 0.42	HII region
103	AGAL327.733-00.387	327.733	-0.387	1.55 ± 0.31	0.1 ± 0.01	3740 ± 1120	47358	1.14 ± 0.08	0.63 ± 0.24	HII region
104	AGAL328.236-00.547	328.236	-0.547	1.25 ± 0.25	0.24 ± 0.02	5607 ± 1680	544204	1.83 ± 0.11	0.86 ± 0.33	Protostellar
105	AGAL328.254-00.532	328.254	-0.532	1.19 ± 0.24	0.19 ± 0.01	4004 ± 1200	47800	2.22 ± 0.17	1.71 ± 0.65	Protostellar
106	AGAL328.256-00.411	328.256	-0.411	0.41 ± 0.08	0.08 ± 0.02	216 ± 60	159	0.62 ± 0.07	0.85 ± 0.32	Protostellar
107	AGAL328.308+00.431	328.308	0.431	2.06 ± 0.41	0.07 ± 0.01	4474 ± 1340	672977	1.64 ± 0.15	1.44 ± 0.55	HII region
108	AGAL328.566-00.534	328.566	-0.534	1.05 ± 0.21	0.08 ± 0.01	1366 ± 410	194534	1.71 ± 0.2	2.61 ± 0.99	HII region
109	AGAL328.809+00.632	328.809	0.632	0.94 ± 0.19	0.12 ± 0.01	1644 ± 490	54037	1.2 ± 0.07	0.96 ± 0.37	Protostellar
110	AGAL329.184-00.314	329.184	-0.314	2.97 ± 0.59	0.13 ± 0.03	17518 ± 5260	185780	1.15 ± 0.08	0.26 ± 0.1	Protostellar
111	AGAL329.337+00.147	329.337	0.147	1.67 ± 0.33	0.08 ± 0.03	3302 ± 990	312328	1.6 ± 0.13	1.5 ± 0.57	HII region
112	AGAL329.424-00.162	329.424	-0.162	1.06 ± 0.21	0.08 ± 0.02	1426 ± 430	10811	1.09 ± 0.11	1.02 ± 0.39	HII region
113	AGAL329.467+00.516	329.467	0.516	0.66 ± 0.13	0.16 ± 0.0	1034 ± 310	2366	1.33 ± 0.11	1.31 ± 0.5	Protostellar
114	AGAL329.469+00.502	329.469	0.502	0.98 ± 0.2	0.13 ± 0.01	1839 ± 550	30321	1.08 ± 0.08	0.72 ± 0.28	Protostellar
115	AGAL329.717+00.806	329.717	0.806	0.67 ± 0.13	0.16 ± 0.01	1071 ± 320	3631	0.86 ± 0.1	0.55 ± 0.21	Protostellar
116	AGAL330.783+00.246	330.783	0.246	0.58 ± 0.12	0.09 ± 0.02	450 ± 130	81	0.65 ± 0.08	0.63 ± 0.24	Protostellar
117	AGAL330.876-00.384	330.876	-0.384	1.01 ± 0.2	0.11 ± 0.01	1713 ± 510	26828	1.49 ± 0.14	1.52 ± 0.58	HII region
118	AGAL330.879-00.367	330.879	-0.367	1.5 ± 0.3	0.1 ± 0.01	3279 ± 980	169697	1.71 ± 0.09	1.56 ± 0.59	HII region
119	AGAL330.954-00.182	330.954	-0.182	1.3 ± 0.26	0.14 ± 0.01	3488 ± 1050	300535	2.52 ± 0.14	2.76 ± 1.05	Protostellar
120	AGAL331.133-00.244	331.133	-0.244	1.23 ± 0.25	0.11 ± 0.01	2568 ± 770	40534	1.89 ± 0.17	2.0 ± 0.76	HII region
121	AGAL331.512-00.102	331.512	-0.102	0.88 ± 0.18	0.22 ± 0.02	2536 ± 760	66890	2.1 ± 0.12	1.78 ± 0.68	HII region
122	AGAL331.521-00.081	331.521	-0.081	1.36 ± 0.27	0.09 ± 0.01	2419 ± 730	336534	1.72 ± 0.13	1.93 ± 0.73	PDR
123	AGAL331.546-00.067	331.546	-0.067	1.41 ± 0.28	0.1 ± 0.01	2828 ± 850	157651	1.64 ± 0.13	1.55 ± 0.59	PDR
124	AGAL331.571-00.229	331.571	-0.229	0.55 ± 0.11	0.06 ± 0.03	254 ± 80	54	0.56 ± 0.09	0.81 ± 0.31	Protostellar
125	AGAL331.626+00.526	331.626	0.526	0.83 ± 0.17	0.07 ± 0.01	710 ± 210	2508	0.88 ± 0.08	1.04 ± 0.4	HII region
126	AGAL331.709+00.602	331.709	0.602	2.59 ± 0.52	0.17 ± 0.02	17205 ± 5160	28582	1.5 ± 0.14	0.39 ± 0.15	Protostellar
127	AGAL331.856-00.126	331.856	-0.126	0.98 ± 0.2	0.08 ± 0.02	1174 ± 350	3459	0.82 ± 0.11	0.66 ± 0.25	HII region
128	AGAL332.094-00.421	332.094	-0.421	1.12 ± 0.22	0.07 ± 0.01	1360 ± 410	37035	1.36 ± 0.12	1.77 ± 0.67	HII region
129	AGAL332.241-00.044	332.241	-0.044	0.93 ± 0.19	0.12 ± 0.01	1599 ± 480	2701	0.88 ± 0.11	0.53 ± 0.2	Protostellar
130	AGAL332.281-00.547	332.281	-0.547	0.87 ± 0.17	0.07 ± 0.01	764 ± 230	1991	0.3 ± 0.06	0.12 ± 0.05	Protostellar
131	AGAL332.296-00.094	332.296	-0.094	1.1 ± 0.22	0.08 ± 0.02	1524 ± 460	20091	0.99 ± 0.08	0.83 ± 0.32	HII region
132	AGAL332.364+00.604	332.364	0.604	0.64 ± 0.13	0.04 ± 0.01	271 ± 80	1374	0.59 ± 0.1	0.95 ± 0.36	Protostellar
133	AGAL332.467-00.522	332.467	-0.522	1.04 ± 0.21	0.09 ± 0.01	1439 ± 430	51735	1.0 ± 0.09	0.84 ± 0.32	Protostellar
134	AGAL332.826-00.549	332.826	-0.549	1.68 ± 0.34	0.12 ± 0.01	5121 ± 1540	171701	2.4 ± 0.1	2.21 ± 0.84	HII region

Table 1 continued

Table 1 (continued)

ID	Sname	l	b	R	Σ	M	L	σ	α_{vir}	evol.phase
		deg	deg	pc	g cm^{-2}	M_{\odot}	L_{\odot}	km s^{-1}		
135	AGAL332.976+00.767	332.976	0.767	0.83 ± 0.17	0.08 ± 0.04	891 ± 270	22670	1.11 ± 0.09	1.34 ± 0.51	PDR
136	AGAL333.013-00.466	333.013	-0.466	0.68 ± 0.14	0.12 ± 0.02	815 ± 240	8004	1.51 ± 0.14	2.22 ± 0.84	PDR
137	AGAL333.018+00.766	333.018	0.766	1.36 ± 0.27	0.16 ± 0.03	4526 ± 1360	32314	1.66 ± 0.09	0.96 ± 0.36	HII region
138	AGAL333.018-00.449	333.018	-0.449	0.7 ± 0.14	0.06 ± 0.01	439 ± 130	24424	1.01 ± 0.11	1.88 ± 0.72	HII region
139	AGAL333.068-00.447	333.068	-0.447	1.62 ± 0.32	0.11 ± 0.01	4350 ± 1310	119693	1.72 ± 0.08	1.28 ± 0.49	Protostellar
140	AGAL333.071-00.399	333.071	-0.399	1.02 ± 0.2	0.13 ± 0.01	1987 ± 600	5546	1.42 ± 0.1	1.19 ± 0.45	Quiescent
141	AGAL333.134-00.431	333.134	-0.431	1.6 ± 0.32	0.19 ± 0.01	7183 ± 2150	245364	2.18 ± 0.21	1.23 ± 0.47	HII region
142	AGAL333.219-00.402	333.219	-0.402	1.25 ± 0.25	0.06 ± 0.01	1366 ± 410	31384	0.85 ± 0.1	0.77 ± 0.29	Protostellar
143	AGAL333.284-00.387	333.284	-0.387	1.37 ± 0.27	0.16 ± 0.01	4563 ± 1370	213003	1.89 ± 0.09	1.24 ± 0.47	HII region
144	AGAL333.299-00.351	333.299	-0.351	1.51 ± 0.3	0.14 ± 0.02	4868 ± 1460	62148	1.61 ± 0.09	0.94 ± 0.36	PDR
145	AGAL333.308-00.366	333.308	-0.366	1.28 ± 0.26	0.16 ± 0.01	3911 ± 1170	149364	1.74 ± 0.08	1.15 ± 0.44	HII region
146	AGAL333.314+00.106	333.314	0.106	0.93 ± 0.19	0.08 ± 0.01	1062 ± 320	3822	1.03 ± 0.15	1.08 ± 0.41	Protostellar
147	AGAL333.524-00.269	333.524	-0.269	1.36 ± 0.27	0.09 ± 0.02	2481 ± 740	20589	1.12 ± 0.12	0.81 ± 0.31	PDR
148	AGAL333.604-00.212	333.604	-0.212	1.99 ± 0.4	0.08 ± 0.01	4534 ± 1360	1040858	1.67 ± 0.08	1.42 ± 0.54	HII region
149	AGAL333.678+00.382	333.678	0.382	0.36 ± 0.07	0.12 ± 0.01	233 ± 70	199	0.82 ± 0.09	1.21 ± 0.46	Protostellar
150	AGAL333.721-00.207	333.721	-0.207	0.97 ± 0.19	0.09 ± 0.03	1232 ± 370	3927	0.83 ± 0.06	0.63 ± 0.24	Protostellar
151	AGAL333.724+00.364	333.724	0.364	0.95 ± 0.19	0.11 ± 0.05	1466 ± 440	10309	1.05 ± 0.08	0.84 ± 0.32	HII region
152	AGAL335.231-00.316	335.231	-0.316	0.35 ± 0.07	0.13 ± 0.02	232 ± 70	108	0.54 ± 0.08	0.51 ± 0.19	Protostellar
153	AGAL335.586-00.291	335.586	-0.291	1.07 ± 0.21	0.14 ± 0.02	2435 ± 730	19543	1.31 ± 0.06	0.87 ± 0.33	Protostellar
154	AGAL335.789+00.174	335.789	0.174	1.23 ± 0.25	0.09 ± 0.02	2123 ± 640	18239	2.25 ± 0.16	3.42 ± 1.3	Protostellar
155	AGAL337.139-00.382	337.139	-0.382	0.54 ± 0.11	0.36 ± 0.03	1543 ± 460	96	1.15 ± 0.1	0.53 ± 0.2	Protostellar
156	AGAL337.406-00.402	337.406	-0.402	0.93 ± 0.19	0.14 ± 0.01	1738 ± 520	565983	1.57 ± 0.06	1.53 ± 0.58	HII region
157	AGAL337.438-00.397	337.438	-0.397	0.97 ± 0.19	0.09 ± 0.02	1292 ± 390	114329	0.81 ± 0.06	0.57 ± 0.22	HII region
158	AGAL337.704-00.054	337.704	-0.054	3.28 ± 0.66	0.21 ± 0.01	33758 ± 10130	138746	1.9 ± 0.16	0.41 ± 0.16	HII region
159	AGAL337.761-00.339	337.761	-0.339	0.88 ± 0.18	0.14 ± 0.01	1613 ± 480	916	1.3 ± 0.08	1.07 ± 0.41	Protostellar
160	AGAL337.844-00.376	337.844	-0.376	0.57 ± 0.11	0.05 ± 0.01	267 ± 80	23335	0.94 ± 0.1	2.21 ± 0.84	HII region
161	AGAL337.916-00.477	337.916	-0.477	0.85 ± 0.17	0.15 ± 0.02	1600 ± 480	101903	1.23 ± 0.07	0.93 ± 0.35	HII region
162	AGAL337.922-00.456	337.922	-0.456	1.16 ± 0.23	0.12 ± 0.02	2489 ± 750	93924	1.28 ± 0.08	0.89 ± 0.34	PDR
163	AGAL338.299+00.572	338.299	0.572	0.64 ± 0.13	0.06 ± 0.01	380 ± 110	4450	0.65 ± 0.09	0.81 ± 0.31	Quiescent
164	AGAL338.926+00.554	338.926	0.554	1.75 ± 0.35	0.25 ± 0.01	11579 ± 3470	74912	2.58 ± 0.13	1.17 ± 0.44	Protostellar
165	AGAL338.926+00.634	338.926	0.634	1.21 ± 0.24	0.1 ± 0.01	2216 ± 660	43493	1.49 ± 0.13	1.41 ± 0.54	Protostellar
166	AGAL338.937-00.492	338.937	-0.492	0.77 ± 0.15	0.08 ± 0.02	733 ± 220	27515	0.84 ± 0.07	0.86 ± 0.33	HII region
167	AGAL339.584-00.127	339.584	-0.127	0.56 ± 0.11	0.15 ± 0.02	688 ± 210	16924	0.95 ± 0.1	0.85 ± 0.32	Protostellar
168	AGAL339.623-00.122	339.623	-0.122	0.66 ± 0.13	0.1 ± 0.02	664 ± 200	4885	0.83 ± 0.07	0.79 ± 0.3	Protostellar
169	AGAL339.924-00.084	339.924	-0.084	0.84 ± 0.17	0.1 ± 0.01	1086 ± 330	21328	2.37 ± 0.19	5.05 ± 1.92	Protostellar
170	AGAL339.949-00.539	339.949	-0.539	2.02 ± 0.4	0.09 ± 0.01	5572 ± 1670	6601	1.06 ± 0.09	0.47 ± 0.18	Protostellar
171	AGAL339.963-00.542	339.963	-0.542	1.71 ± 0.34	0.06 ± 0.01	2784 ± 840	9142	0.91 ± 0.09	0.6 ± 0.23	PDR
172	AGAL340.054-00.244	340.054	-0.244	1.29 ± 0.26	0.1 ± 0.01	2428 ± 730	687354	1.99 ± 0.13	2.45 ± 0.93	Protostellar
173	AGAL340.248-00.374	340.248	-0.374	1.63 ± 0.33	0.13 ± 0.01	5277 ± 1580	30362	1.37 ± 0.08	0.68 ± 0.26	HII region
174	AGAL340.249-00.046	340.249	-0.046	2.8 ± 0.56	0.08 ± 0.02	9777 ± 2930	48002	1.34 ± 0.11	0.6 ± 0.23	HII region
175	AGAL340.256-00.226	340.256	-0.226	0.67 ± 0.13	0.14 ± 0.03	932 ± 280	2165	1.21 ± 0.14	1.23 ± 0.47	Quiescent
176	AGAL340.274-00.211	340.274	-0.211	0.87 ± 0.17	0.16 ± 0.03	1762 ± 530	12373	1.45 ± 0.12	1.21 ± 0.46	PDR
177	AGAL340.401-00.381	340.401	-0.381	0.94 ± 0.19	0.16 ± 0.01	2071 ± 620	13385	1.24 ± 0.12	0.81 ± 0.31	HII region
178	AGAL340.746-01.001	340.746	-1.001	0.73 ± 0.15	0.12 ± 0.02	931 ± 280	4655	1.12 ± 0.09	1.13 ± 0.43	Protostellar
179	AGAL340.768-01.012	340.768	-1.012	0.37 ± 0.07	0.23 ± 0.01	470 ± 140	7070	0.88 ± 0.06	0.7 ± 0.27	Protostellar
180	AGAL340.784-01.016	340.784	-1.016	0.93 ± 0.19	0.1 ± 0.01	1277 ± 380	80810	1.31 ± 0.07	1.45 ± 0.55	HII region

Table 1 continued

Table 1 (continued)

ID	Sname	l	b	R	Σ	M	L	σ	α_{vir}	evol.phase
		deg	deg	pc	g cm^{-2}	M_{\odot}	L_{\odot}	km s^{-1}		
181	AGAL340.969-01.021	340.969	-1.021	0.56 ± 0.11	0.22 ± 0.03	1060 ± 320	5370	1.64 ± 0.11	1.66 ± 0.63	Protostellar
182	AGAL341.196-00.221	341.196	-0.221	0.68 ± 0.14	0.1 ± 0.02	716 ± 210	1309	0.31 ± 0.06	0.11 ± 0.04	Quiescent
183	AGAL341.216-00.236	341.216	-0.236	0.96 ± 0.19	0.09 ± 0.01	1194 ± 360	12152	1.0 ± 0.07	0.94 ± 0.36	Protostellar
184	AGAL341.217-00.212	341.217	-0.212	0.7 ± 0.14	0.12 ± 0.01	868 ± 260	4698	1.11 ± 0.12	1.16 ± 0.44	Protostellar
185	AGAL341.219-00.259	341.219	-0.259	0.72 ± 0.14	0.15 ± 0.01	1162 ± 350	1549	1.11 ± 0.1	0.88 ± 0.33	Protostellar
186	AGAL341.236-00.271	341.236	-0.271	0.77 ± 0.15	0.13 ± 0.01	1171 ± 350	1691	1.33 ± 0.1	1.35 ± 0.51	Protostellar
187	AGAL341.266-00.302	341.266	-0.302	0.84 ± 0.17	0.17 ± 0.02	1868 ± 560	2826	1.52 ± 0.1	1.22 ± 0.46	HII region
188	AGAL341.932-00.174	341.932	-0.174	3.91 ± 0.78	0.25 ± 0.01	57426 ± 17230	56885	1.44 ± 0.12	0.16 ± 0.06	HII region
189	AGAL341.942-00.166	341.942	-0.166	4.08 ± 0.82	0.26 ± 0.01	64979 ± 19490	65464	1.38 ± 0.12	0.14 ± 0.05	HII region
190	AGAL342.484+00.182	342.484	0.182	3.36 ± 0.67	0.08 ± 0.01	13955 ± 4190	41646	0.74 ± 0.09	0.15 ± 0.06	Protostellar
191	AGAL342.708+00.126	342.708	0.126	1.27 ± 0.25	0.14 ± 0.03	3280 ± 980	283084	1.42 ± 0.08	0.9 ± 0.34	HII region
192	AGAL343.128-00.062	343.128	-0.062	0.97 ± 0.19	0.13 ± 0.01	1863 ± 560	34266	1.93 ± 0.08	2.25 ± 0.85	Protostellar
193	AGAL343.398-00.329	343.398	-0.329	0.58 ± 0.12	0.07 ± 0.03	347 ± 100	255	0.48 ± 0.08	0.44 ± 0.17	Protostellar
194	AGAL343.501+00.026	343.501	0.026	0.62 ± 0.12	0.07 ± 0.01	415 ± 120	39954	1.45 ± 0.14	3.67 ± 1.39	Protostellar
195	AGAL343.521-00.519	343.521	-0.519	0.76 ± 0.15	0.12 ± 0.03	1058 ± 320	2944	1.2 ± 0.09	1.21 ± 0.46	HII region
196	AGAL343.528-00.507	343.528	-0.507	0.4 ± 0.08	0.12 ± 0.02	283 ± 80	876	1.12 ± 0.11	2.07 ± 0.79	Protostellar
197	AGAL343.721-00.224	343.721	-0.224	0.68 ± 0.14	0.07 ± 0.01	495 ± 150	60341	0.78 ± 0.09	0.97 ± 0.37	HII region
198	AGAL343.756-00.164	343.756	-0.164	0.8 ± 0.16	0.17 ± 0.01	1668 ± 500	6442	1.04 ± 0.07	0.61 ± 0.23	Protostellar
199	AGAL343.779-00.236	343.779	-0.236	0.54 ± 0.11	0.08 ± 0.02	362 ± 110	902	0.99 ± 0.1	1.71 ± 0.65	Protostellar
200	AGAL344.221-00.594	344.221	-0.594	0.61 ± 0.12	0.17 ± 0.02	965 ± 290	16829	1.27 ± 0.09	1.19 ± 0.45	HII region
201	AGAL344.424+00.046	344.424	0.046	2.18 ± 0.44	0.09 ± 0.01	6482 ± 1940	123641	1.14 ± 0.08	0.5 ± 0.19	HII region
202	AGAL344.726-00.542	344.726	-0.542	0.53 ± 0.11	0.07 ± 0.03	278 ± 80	5	0.47 ± 0.08	0.49 ± 0.19	Quiescent
203	AGAL344.990-00.274	344.99	-0.274	0.85 ± 0.17	0.09 ± 0.02	969 ± 290	8279	1.4 ± 0.11	2.01 ± 0.76	HII region
204	AGAL345.003-00.224	345.003	-0.224	1.27 ± 0.25	0.18 ± 0.02	4297 ± 1290	39810	1.34 ± 0.13	0.62 ± 0.24	Protostellar
205	AGAL345.263-00.417	345.263	-0.417	0.46 ± 0.09	0.06 ± 0.01	192 ± 60	904	0.74 ± 0.08	1.53 ± 0.58	HII region
206	AGAL345.408-00.952	345.408	-0.952	0.61 ± 0.12	0.09 ± 0.02	480 ± 140	217887	2.04 ± 0.13	6.08 ± 2.31	HII region
207	AGAL345.488+00.314	345.488	0.314	1.11 ± 0.22	0.19 ± 0.02	3419 ± 1030	39230	1.63 ± 0.11	1.0 ± 0.38	HII region
208	AGAL345.504+00.347	345.504	0.347	1.24 ± 0.25	0.13 ± 0.0	2911 ± 870	35200	1.22 ± 0.06	0.73 ± 0.28	HII region
209	AGAL345.718+00.817	345.718	0.817	0.81 ± 0.16	0.14 ± 0.01	1332 ± 400	1084	0.92 ± 0.05	0.6 ± 0.23	Protostellar
210	AGAL346.369-00.647	346.369	-0.647	0.15 ± 0.03	0.08 ± 0.0	27 ± 10	4479	0.23 ± 0.02	0.33 ± 0.13	Protostellar
211	AGAL347.872-00.311	347.872	-0.311	1.86 ± 0.37	0.08 ± 0.01	4126 ± 1240	13250	0.92 ± 0.11	0.45 ± 0.17	HII region
212	AGAL348.171+00.466	348.171	0.466	0.16 ± 0.03	0.21 ± 0.01	80 ± 20	541	0.96 ± 0.06	2.13 ± 0.81	Protostellar
213	AGAL348.183+00.482	348.183	0.482	0.53 ± 0.11	0.17 ± 0.01	697 ± 210	503564	0.97 ± 0.04	0.83 ± 0.32	PDR
214	AGAL348.376+00.524	348.376	0.524	0.27 ± 0.05	0.17 ± 0.02	194 ± 60	34	0.69 ± 0.05	0.79 ± 0.3	Protostellar
215	AGAL348.383+00.537	348.383	0.537	0.22 ± 0.04	0.15 ± 0.01	103 ± 30	12	0.52 ± 0.05	0.65 ± 0.25	Quiescent
216	AGAL348.549-00.979	348.549	-0.979	1.08 ± 0.22	0.15 ± 0.01	2595 ± 780	12293	2.0 ± 0.15	1.94 ± 0.74	Protostellar
217	AGAL348.579-00.919	348.579	-0.919	1.03 ± 0.21	0.18 ± 0.01	2887 ± 870	2027	1.09 ± 0.12	0.49 ± 0.19	Protostellar
218	AGAL348.698-01.027	348.698	-1.027	0.74 ± 0.15	0.16 ± 0.01	1349 ± 400	11739	1.53 ± 0.05	1.5 ± 0.57	HII region
219	AGAL348.701-01.042	348.701	-1.042	0.68 ± 0.14	0.28 ± 0.0	1943 ± 580	61235	1.82 ± 0.05	1.34 ± 0.51	HII region
220	AGAL348.726-01.039	348.726	-1.039	1.57 ± 0.31	0.12 ± 0.02	4269 ± 1280	97259	1.7 ± 0.07	1.24 ± 0.47	HII region
221	AGAL348.759-00.946	348.759	-0.946	1.33 ± 0.27	0.2 ± 0.02	5204 ± 1560	2253	1.41 ± 0.1	0.59 ± 0.22	Protostellar

NOTE—Physical properties of the 221 clumps. Col.2-4: Clump name and coordinates; Col.5-7: Clump radius, average mass surface density, and mass; Col.8: Clump luminosity; Col.9-10: Clump velocity dispersion and virial parameter; Col.11: the evolutionary phase of clumps. Three dots in the clump luminosity column signify that the luminosity data for these clumps was not collected. Note that the clump radius and average mass surface density are retrieved from Guzmán et al. (2015), while the clump luminosity is obtained from Contreras et al. (2017) and Urquhart et al. (2022). The remaining derived parameters are carried out in this work.

REFERENCES

- Ballesteros-Paredes, J., Hartmann, L. W., Vázquez-Semadeni, E., Heitsch, F., & Zamora-Avilés, M. A. 2011a, *MNRAS*, 411, 65, doi: [10.1111/j.1365-2966.2010.17657.x](https://doi.org/10.1111/j.1365-2966.2010.17657.x)
- Ballesteros-Paredes, J., Vázquez-Semadeni, E., Gazol, A., et al. 2011b, *MNRAS*, 416, 1436, doi: [10.1111/j.1365-2966.2011.19141.x](https://doi.org/10.1111/j.1365-2966.2011.19141.x)
- Ballesteros-Paredes, J., Vázquez-Semadeni, E., Palau, A., & Klessen, R. S. 2018, *MNRAS*, 479, 2112, doi: [10.1093/mnras/sty1515](https://doi.org/10.1093/mnras/sty1515)
- Ballesteros-Paredes, J., André, P., Hennebelle, P., et al. 2020, *SSRv*, 216, 76, doi: [10.1007/s11214-020-00698-3](https://doi.org/10.1007/s11214-020-00698-3)
- Bertoldi, F., & McKee, C. F. 1992, *ApJ*, 395, 140, doi: [10.1086/171638](https://doi.org/10.1086/171638)
- Carey, S. J., Noriega-Crespo, A., Mizuno, D. R., et al. 2009, *PASP*, 121, 76, doi: [10.1086/596581](https://doi.org/10.1086/596581)
- Chambers, E. T., Jackson, J. M., Rathborne, J. M., & Simon, R. 2009, *ApJS*, 181, 360, doi: [10.1088/0067-0049/181/2/360](https://doi.org/10.1088/0067-0049/181/2/360)
- Churchwell, E., Babler, B. L., Meade, M. R., et al. 2009, *PASP*, 121, 213, doi: [10.1086/597811](https://doi.org/10.1086/597811)
- Contreras, Y., Rathborne, J. M., Guzman, A., et al. 2017, *MNRAS*, 466, 340, doi: [10.1093/mnras/stw3110](https://doi.org/10.1093/mnras/stw3110)
- Elmegreen, B. G. 1993, *ApJL*, 419, L29, doi: [10.1086/187129](https://doi.org/10.1086/187129)
- Goldbaum, N. J., Krumholz, M. R., Matzner, C. D., & McKee, C. F. 2011, *ApJ*, 738, 101, doi: [10.1088/0004-637X/738/1/101](https://doi.org/10.1088/0004-637X/738/1/101)
- Gong, M., & Ostriker, E. C. 2015, *ApJ*, 806, 31, doi: [10.1088/0004-637X/806/1/31](https://doi.org/10.1088/0004-637X/806/1/31)
- González-Samaniego, A., Vázquez-Semadeni, E., González, R. F., & Kim, J. 2014, *MNRAS*, 440, 2357, doi: [10.1093/mnras/stu400](https://doi.org/10.1093/mnras/stu400)
- Gu, Q., & Li, H.-b. 2019, *ApJL*, 871, L15, doi: [10.3847/2041-8213/aafdb1](https://doi.org/10.3847/2041-8213/aafdb1)
- Guerrero-Gamboa, R., & Vázquez-Semadeni, E. 2020, *ApJ*, 903, 136, doi: [10.3847/1538-4357/abbaf1](https://doi.org/10.3847/1538-4357/abbaf1)
- Guzmán, A. E., Sanhueza, P., Contreras, Y., et al. 2015, *ApJ*, 815, 130, doi: [10.1088/0004-637X/815/2/130](https://doi.org/10.1088/0004-637X/815/2/130)
- Hartmann, L., Ballesteros-Paredes, J., & Bergin, E. A. 2001, *ApJ*, 562, 852, doi: [10.1086/323863](https://doi.org/10.1086/323863)
- Hartmann, L., & Burkert, A. 2007, *ApJ*, 654, 988, doi: [10.1086/509321](https://doi.org/10.1086/509321)
- Hennebelle, P., & Falgarone, E. 2012, *A&A Rv*, 20, 55, doi: [10.1007/s00159-012-0055-y](https://doi.org/10.1007/s00159-012-0055-y)
- Heyer, M., Krawczyk, C., Duval, J., & Jackson, J. M. 2009, *ApJ*, 699, 1092, doi: [10.1088/0004-637X/699/2/1092](https://doi.org/10.1088/0004-637X/699/2/1092)
- Heyer, M. H., & Brunt, C. M. 2004, *ApJL*, 615, L45, doi: [10.1086/425978](https://doi.org/10.1086/425978)
- Holm-Hansen, C., Putman, M. E., & Kim, D. A. 2023, arXiv e-prints, arXiv:2312.09164, doi: [10.48550/arXiv.2312.09164](https://doi.org/10.48550/arXiv.2312.09164)
- Ibáñez-Mejía, J. C., Mac Low, M.-M., & Klessen, R. S. 2022, *ApJ*, 925, 196, doi: [10.3847/1538-4357/ac3b58](https://doi.org/10.3847/1538-4357/ac3b58)
- Ibáñez-Mejía, J. C., Mac Low, M.-M., Klessen, R. S., & Baczynski, C. 2016, *ApJ*, 824, 41, doi: [10.3847/0004-637X/824/1/41](https://doi.org/10.3847/0004-637X/824/1/41)
- Inoue, T., & Fukui, Y. 2013a, *ApJL*, 774, L31, doi: [10.1088/2041-8205/774/2/L31](https://doi.org/10.1088/2041-8205/774/2/L31)
- . 2013b, *ApJL*, 774, L31, doi: [10.1088/2041-8205/774/2/L31](https://doi.org/10.1088/2041-8205/774/2/L31)
- Jackson, J. M., Rathborne, J. M., Foster, J. B., et al. 2013, *PASA*, 30, e057, doi: [10.1017/pasa.2013.37](https://doi.org/10.1017/pasa.2013.37)
- Kauffmann, J., Pillai, T., & Goldsmith, P. F. 2013, *ApJ*, 779, 185, doi: [10.1088/0004-637X/779/2/185](https://doi.org/10.1088/0004-637X/779/2/185)
- Knee, L. B. G., & Sandell, G. 2000, *A&A*, 361, 671
- Kritsuk, A. G., Norman, M. L., & Wagner, R. 2011, *ApJL*, 727, L20, doi: [10.1088/2041-8205/727/1/L20](https://doi.org/10.1088/2041-8205/727/1/L20)
- Larson, R. B. 1981, *MNRAS*, 194, 809, doi: [10.1093/mnras/194.4.809](https://doi.org/10.1093/mnras/194.4.809)
- Li, H.-b., Fang, M., Henning, T., & Kainulainen, J. 2013, *MNRAS*, 436, 3707, doi: [10.1093/mnras/stt1849](https://doi.org/10.1093/mnras/stt1849)
- Li, S., Sanhueza, P., Zhang, Q., et al. 2023, *ApJ*, 949, 109, doi: [10.3847/1538-4357/acc58f](https://doi.org/10.3847/1538-4357/acc58f)
- Liu, H.-L., Sanhueza, P., Liu, T., et al. 2020, *ApJ*, 901, 31, doi: [10.3847/1538-4357/abadfe](https://doi.org/10.3847/1538-4357/abadfe)
- Liu, H.-L., Tej, A., Liu, T., et al. 2022a, *MNRAS*, 510, 5009, doi: [10.1093/mnras/stab2757](https://doi.org/10.1093/mnras/stab2757)
- . 2022b, *MNRAS*, 511, 4480, doi: [10.1093/mnras/stac378](https://doi.org/10.1093/mnras/stac378)
- . 2023, *MNRAS*, 522, 3719, doi: [10.1093/mnras/stad047](https://doi.org/10.1093/mnras/stad047)
- Liu, X., Liu, T., Lu, X., Luo, Q. A., & Liu, H.-L. 2024, *ApJ*, to be submitted
- Lu, X., Zhang, Q., Liu, H. B., et al. 2018, *ApJ*, 855, 9, doi: [10.3847/1538-4357/aaad11](https://doi.org/10.3847/1538-4357/aaad11)
- Matzner, C. D. 2002, *ApJ*, 566, 302, doi: [10.1086/338030](https://doi.org/10.1086/338030)
- Molinari, S., Pezzuto, S., Cesaroni, R., et al. 2008, *A&A*, 481, 345, doi: [10.1051/0004-6361:20078661](https://doi.org/10.1051/0004-6361:20078661)
- Motte, F., Bontemps, S., & Louvet, F. 2018, *ARA&A*, 56, 41, doi: [10.1146/annurev-astro-091916-055235](https://doi.org/10.1146/annurev-astro-091916-055235)
- Mouschovias, T. C., Tassis, K., & Kunz, M. W. 2006, *ApJ*, 646, 1043, doi: [10.1086/500125](https://doi.org/10.1086/500125)
- Myers, P. C., & Goodman, A. A. 1988, *ApJ*, 329, 392, doi: [10.1086/166385](https://doi.org/10.1086/166385)
- Ohashi, S., Sanhueza, P., Chen, H.-R. V., et al. 2016, *ApJ*, 833, 209, doi: [10.3847/1538-4357/833/2/209](https://doi.org/10.3847/1538-4357/833/2/209)
- Ostriker, E. C., & Shetty, R. 2011, *ApJ*, 731, 41, doi: [10.1088/0004-637X/731/1/41](https://doi.org/10.1088/0004-637X/731/1/41)
- Padoan, P., Pan, L., Haugbølle, T., & Nordlund, Å. 2016, *ApJ*, 822, 11, doi: [10.3847/0004-637X/822/1/11](https://doi.org/10.3847/0004-637X/822/1/11)

- Padoan, P., Pan, L., Juvela, M., Haugbølle, T., & Nordlund, Å. 2020, *ApJ*, 900, 82, doi: [10.3847/1538-4357/abaa47](https://doi.org/10.3847/1538-4357/abaa47)
- Pan, L., Padoan, P., & Nordlund, Å. 2019, *ApJ*, 881, 155, doi: [10.3847/1538-4357/ab2ed6](https://doi.org/10.3847/1538-4357/ab2ed6)
- Pan, S., Liu, H.-L., & Qin, S.-L. 2024, *ApJ*, 960, 76, doi: [10.3847/1538-4357/ad10ac](https://doi.org/10.3847/1538-4357/ad10ac)
- Peretto, N., André, P., & Belloche, A. 2006, *A&A*, 445, 979, doi: [10.1051/0004-6361:20053324](https://doi.org/10.1051/0004-6361:20053324)
- Peretto, N., Rigby, A. J., Louvet, F., et al. 2023, *MNRAS*, 525, 2935, doi: [10.1093/mnras/stad2453](https://doi.org/10.1093/mnras/stad2453)
- Peretto, N., Fuller, G. A., Duarte-Cabral, A., et al. 2013, *A&A*, 555, A112, doi: [10.1051/0004-6361/201321318](https://doi.org/10.1051/0004-6361/201321318)
- Planck Collaboration, Ade, P. A. R., Aghanim, N., et al. 2016, *A&A*, 586, A138, doi: [10.1051/0004-6361/201525896](https://doi.org/10.1051/0004-6361/201525896)
- Quillen, A. C., Thorndike, S. L., Cunningham, A., et al. 2005, *ApJ*, 632, 941, doi: [10.1086/444410](https://doi.org/10.1086/444410)
- Rathborne, J. M., Whitaker, J. S., Jackson, J. M., et al. 2016, *PASA*, 33, e030, doi: [10.1017/pasa.2016.23](https://doi.org/10.1017/pasa.2016.23)
- Roman-Duval, J., Jackson, J. M., Heyer, M., Rathborne, J., & Simon, R. 2010, *ApJ*, 723, 492, doi: [10.1088/0004-637X/723/1/492](https://doi.org/10.1088/0004-637X/723/1/492)
- Schneider, N., André, P., Könyves, V., et al. 2013, *ApJL*, 766, L17, doi: [10.1088/2041-8205/766/2/L17](https://doi.org/10.1088/2041-8205/766/2/L17)
- Schneider, N., Ossenkopf, V., Csengeri, T., et al. 2015, *A&A*, 575, A79, doi: [10.1051/0004-6361/201423569](https://doi.org/10.1051/0004-6361/201423569)
- Schuller, F., Menten, K. M., Contreras, Y., et al. 2009, *A&A*, 504, 415, doi: [10.1051/0004-6361/200811568](https://doi.org/10.1051/0004-6361/200811568)
- Soler, J. D., Alves, F., Boulanger, F., et al. 2016, *A&A*, 596, A93, doi: [10.1051/0004-6361/201628996](https://doi.org/10.1051/0004-6361/201628996)
- Solomon, P. M., Rivolo, A. R., Barrett, J., & Yahil, A. 1987, *ApJ*, 319, 730, doi: [10.1086/165493](https://doi.org/10.1086/165493)
- Traficante, A., Duarte-Cabral, A., Elia, D., et al. 2018, *MNRAS*, 477, 2220, doi: [10.1093/mnras/sty798](https://doi.org/10.1093/mnras/sty798)
- Urquhart, J. S., Moore, T. J. T., Csengeri, T., et al. 2014, *MNRAS*, 443, 1555, doi: [10.1093/mnras/stu1207](https://doi.org/10.1093/mnras/stu1207)
- Urquhart, J. S., König, C., Giannetti, A., et al. 2018, *MNRAS*, 473, 1059, doi: [10.1093/mnras/stx2258](https://doi.org/10.1093/mnras/stx2258)
- Urquhart, J. S., Wells, M. R. A., Pillai, T., et al. 2022, *MNRAS*, 510, 3389, doi: [10.1093/mnras/stab3511](https://doi.org/10.1093/mnras/stab3511)
- Vázquez-Semadeni, E., Gómez, G. C., Jappsen, A. K., et al. 2007, *ApJ*, 657, 870, doi: [10.1086/510771](https://doi.org/10.1086/510771)
- Vázquez-Semadeni, E., Gómez, G. C., Jappsen, A. K., Ballesteros-Paredes, J., & Klessen, R. S. 2009, *ApJ*, 707, 1023, doi: [10.1088/0004-637X/707/2/1023](https://doi.org/10.1088/0004-637X/707/2/1023)
- Vázquez-Semadeni, E., González-Samaniego, A., & Colín, P. 2017, *MNRAS*, 467, 1313, doi: [10.1093/mnras/stw3229](https://doi.org/10.1093/mnras/stw3229)
- Vázquez-Semadeni, E., Palau, A., Ballesteros-Paredes, J., Gómez, G. C., & Zamora-Avilés, M. 2019, *MNRAS*, 490, 3061, doi: [10.1093/mnras/stz2736](https://doi.org/10.1093/mnras/stz2736)
- Yang, D., Liu, H.-L., Tej, A., et al. 2023, *ApJ*, 953, 40, doi: [10.3847/1538-4357/acdf42](https://doi.org/10.3847/1538-4357/acdf42)
- Zhou, J.-W., Liu, T., Evans, N. J., et al. 2022, *MNRAS*, 514, 6038, doi: [10.1093/mnras/stac1735](https://doi.org/10.1093/mnras/stac1735)